J. Fluid Mech. (2007), *vol.* 589, *pp.* 183–213.
doi:10.1017/S0022112007007690 Printed in the United Kingdom

Effect of gravity modulation on the stability of a horizontal double-diffusive layer

YOUMIN YU, CHO LIK CHAN AND C. F. CHEN

Department of Aerospace and Mechanical Engineering, University of Arizona
Tucson, AZ 85721, USA

(Received 15 August 2006 and in revised form 17 May 2007)

The instability characteristics of a horizontal stably stratified fluid layer being heated from below, including its subsequent nonlinear evolution under steady and modulated gravity, have been investigated by experiments and two-dimensional numerical simulations. The critical condition at instability onset is also checked using linear stability analysis. The fluid is contained in a horizontal test tank with an initial stable solute gradient and a constant-temperature gradient imposed by heating from below. Because of the non-diffusive boundaries, the vertical solute gradient slowly decreases and, eventually, the layer becomes unstable. From the time of the onset of instability, the critical solute Rayleigh number is determined. For the experiments with modulated gravity, the tank is fixed onto a platform that oscillates vertically at 1 Hz with an amplitude of 10 cm. The experiment is designed such that no internal wave mode of instability can be excited. The experimental results show that gravity modulation destabilizes the system slightly by increasing the solute Rayleigh number at onset by 8.4 % and causes the oscillation frequency at onset to increase by 32.6 %. Linear stability analysis and two-dimensional numerical simulations for the steady gravity case yield results that are in good agreement with the experiment. For the gravity modulation case, linear stability results do not show any effect of gravity modulation at the frequency of 1 Hz. Numerical simulation results do show increases in both the onset solute Rayleigh number and the oscillation frequency; however, their values are smaller than those obtained in the experiment. The characteristics of the internal wave mode of instability are explored by numerical simulations of a stably stratified solute fluid layer under gravity modulation. The interference effects between the internal wave mode and double-diffusive mode of instabilities are studied by imposing an adverse temperature gradient on the stratified layer.

1. Introduction

The stability of a horizontal fluid layer with an imposed temperature gradient confined within rigid boundaries under gravity oscillation was first examined by Gresho & Sani (1970) and by Gershuni, Zhukhovitskii & Iurkov (1970). Their results show that the stability of the layer being heated from below is enhanced by gravity modulation; but for the case of heating from above, the layer is destabilized. In both cases, fluid motion at the onset of instability can be either in the synchronous or the subharmonic mode. With the advent of orbiting space laboratories capable of providing micro-gravity experiments in materials processing, there is a need to consider the additional effect of mass diffusion on the instability mechanism of such a layer. Saunders *et al.* (1992) studied the effect of gravity modulation on the stability

of a horizontal double-diffusive layer. They considered a fluid layer of stress-free boundaries with linear temperature and solute concentration distributions that would generate instabilities either in the finger or the diffusive mode. For the diffusive case, the instability regions at higher amplitudes of gravity modulation appear in a series of resonant bands in which the instabilities oscillate alternately in the subharmonic and synchronous mode. However, within the fundamental band of instability, the oscillatory onset of convection is in complex conjugate pairs.

Experiments on the response of Rayleigh–Bénard convection to gravity modulation were carried out by Rogers *et al.* (2005). Their interest is in the study of the complex-ordered patterns of convection generated under such conditions. The experiments were carried out in a circular horizontal layer of pressurized carbon dioxide (CO_2) with heating from below. Their linear analysis and nonlinear calculations included cases with heating from above. They noted that for such cases, internal waves can be excited, and when these modes are resonantly coupled to the modulated gravity, instability can be generated.

Shirtcliffe (1967, 1969) carried out the first experimental investigations of double-diffusive instability by heating a stably stratified sugar solution from below. The thermal and solutal Rayleigh numbers at onset were determined by using the measured sugar gradient and the computed temperature profile. The oscillation of the instability was determined by differential temperature measurements. His results agreed well with the linear stability predictions of Nield (1967). Wright & Loehrke (1976) used a test tank with porous metal boundaries at the top and bottom through which both salt and heat could diffuse. Their experimental results agreed well with those predicted by the linear stability theory for a fluid layer with constant values of temperature and solute concentration at the two boundaries.

For the present experiments, it is difficult to adapt the apparatus used by Wright & Loehrke (1976) to be mounted on an oscillating platform. Instead, we use the fact that the concentration gradient decays slowly owing to the non-diffusive top and bottom boundaries to help us to determine the critical state. We fill a horizontal tank with stably stratified solute solution, and then apply an adverse temperature gradient that is subcritical with respect to the initial solute gradient. We wait for the slow decay of the solute gradient to render the fluid layer unstable. This procedure is equally applicable for the steady and modulated gravity cases. In the following, we first describe the experimental apparatus and procedure, then the experimental results including the methods we used to determine the oscillation frequency at onset, followed by a short section on the linear stability results for the experimental nonlinear solute distribution. Next, we present the methods and results of two-dimensional simulations of the experiments, including the time rate of change of the total kinetic energy of the fluid as it passes through the onset stage to the fully saturated nonlinear state. Lastly, we present simulation results that illustrate the interference between the internal wave mode of instability and the double-diffusive instability.

2. Experimental apparatus and procedure

Experiments were conducted in a shallow tank with interior dimensions of 10.8 cm (W) $\times$ 1 cm (H) $\times$ 5.4 cm wide. For flow visualization and particle image velocimetry (PIV) application purposes, the tank is transparent except for the bottom. All sidewalls are made of Plexiglas. The top of the tank is a sealed Plexiglas box with a 0.1 cm thick sapphire bottom plate for heat transfer purposes. Temperature in the box is maintained constant by circulating transparent glycerine–water solution

from a constant-temperature bath. The bottom boundary of the tank is made of a 1.27 cm thick copper plate with sealed passages to allow the circulation of constant-temperature fluid from another bath. The temperature of the copper plate is measured by an embedded thermocouple. The temperature of the sapphire plate wetted by the test fluid is determined by heat transfer calculation using the measured temperature and volume flow rate of the glycerine–water solution and the temperature of the bottom wall.

An oscillating platform is used to impart gravity modulation in the vertical direction. By using a Scotch yoke mechanism, the rotary motion of a flywheel driven by a d.c. motor is transformed into the sinusoidal vertical oscillation of a vertical shaft, to which a platform is firmly attached. The vertical stroke is 10 cm. The test tank and a digital movie camera are mounted on the platform. The desired frequency of gravity modulation is controlled by adjusting the current input to the d.c. motor, and the amplitude of the modulation is proportional to the square of the frequency. When the platform is oscillating at 1.0 Hz, the maximum amplitude of the platform acceleration is $0.41g$, where g is gravity at sea level. An accelerometer is attached to the platform so that its acceleration is continuously monitored during the experiment. All the signals from the thermocouples and the accelerometer are streamed into a personal computer through hardware configuration. These signals are then displayed, processed, and saved with a code developed in LabVIEW.

For flow visualization and PIV purposes, the test fluid is seeded with 10 μm polycrystalline particles. The light from a Coherent 4 W laser is rendered into a sheet approximately 1 mm in thickness by a cylindrical lens and is then deflected downward, illuminating the mid-plane of the test tank. The motions of the particles in this plane are captured by the digital camera and streamed into a Macintosh computer as movie clips. From these clips, streaklines can be constructed, and fluid velocities can be evaluated by PIV software.

The following three factors are considered when determining the initial solute gradient of the fluid. (i) The gradient must be large enough so the fluid layer is subcritical under the imposed ΔT. (ii) The onset of double-diffusive instability occurs at approximately 10 °C ΔT in order to limit the effect of viscosity variation within the fluid. (iii) The initial density gradient should be stable with respect to internal wave instability when it is under a gravity modulation of 1 Hz. For a continuously stratified fluid, Sekerzh-Zen'kovitch (1983) has shown by linear stability analysis that parametric instability of such a layer is excited when it is oscillated at a frequency less than $2N$, where N is the buoyancy frequency. Benielli & Sommeria (1998) carried out experiments on parametric instability in continuously stratified salt solution by vertical oscillation. The value of $2N$ for the fluid is 0.462 Hz. They showed that for oscillation frequencies larger than 0.462 Hz, no instability is observed up to an oscillation amplitude of $\sim 0.1g$. However, when the forcing frequency is increased to 3.47 Hz, the free-surface mode of instability is excited. When the frequency is reduced to $0.432\,\text{Hz} < 2N$, internal waves in the subharmonic mode are excited.

With these considerations in mind, we use 0.0 wt % and 2.0 wt % ethanol–water solutions to establish the stratified fluid layer. The thermophysical properties of the fluid layer are evaluated for the mixed 1.0 wt % ethanol–water solution at 22.5 °C. The kinematic viscosity $\nu = 1.005 \times 10^{-2}\,\text{cm}^2\,\text{s}^{-1}$; thermal and solutal diffusivity are $\kappa_T = 1.429 \times 10^{-3}\,\text{cm}^2\,\text{s}^{-1}$ and $\kappa_S = 1.208 \times 10^{-5}\,\text{cm}^2\,\text{s}^{-1}$, respectively; the thermal expansion coefficient is $\beta_T = -\rho_0^{-1}\partial\rho/\partial T = 2.330 \times 10^{-4}\,\text{K}^{-1}$ and the solutal counterpart is $\beta_S = -\rho_0^{-1}\partial\rho/\partial S = -1.863 \times 10^{-3}\,\%^{-1}$ (Landolt & Bornstein 1989); the Prandtl number $Pr = \nu/\kappa_T = 7.033$, and the Lewis number $Le = \kappa_T/\kappa_S = 118.3$.

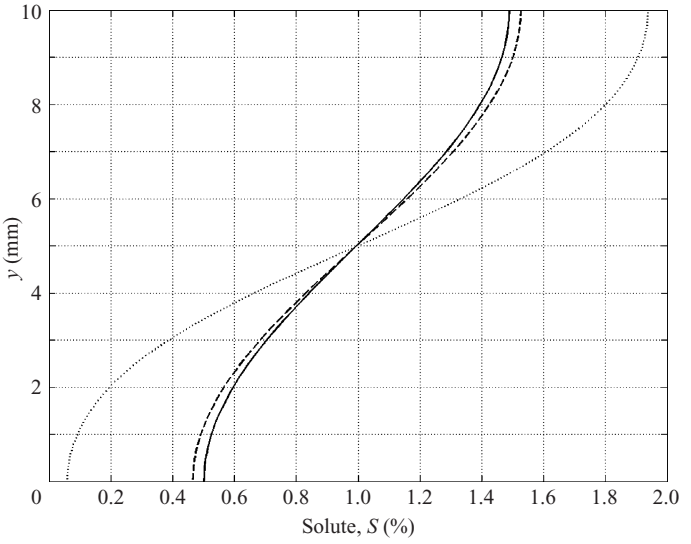

FIGURE 1. Solute distributions at $\cdots$, $t = 0$, $---$, 86 min, and ———, 95 min into the experiment.

From these values, the thermal Rayleigh number $Ra_T = g\beta_T \Delta T H^3/\kappa_T \nu$ and the solute Rayleigh number $Ra_s = g\beta_S \Delta S H^3/\kappa_T \nu$ can be evaluated, where ΔT and ΔS are the temperature and solute differences between the bottom and the top of the tank. For our choice of the initial stratification, no internal Faraday waves can be excited. However, in the numerical simulations, we selected an example with gravity modulation less than $2N$ and show the interactions between the internal Faraday waves and double-diffusive instability.

To establish the solute gradient, the lower half of the test tank is first filled with pure water. Then 2.0 wt % ethanol–water solution is slowly injected onto a thin slat of balsa wood floating on the water in order to minimize mixing. When the filling is complete, the balsa wood is carefully removed and the top transparent heat transfer box is secured to the test tank by external clamps. Then the filled tank is left standing for 30 min to allow diffusion of ethanol to smooth out the gradient. At this time, a 10 K temperature difference is imposed across the tank. This marks the beginning of the experiment designated as $t = 0$. Recorded data indicate that the temperatures of the top and lower boundaries reach their steady state values in less than 1.5 min after the circulating baths are activated. A linear temperature distribution is established within the test tank in less than 3 min. The one-dimensional diffusion equation is numerically integrated to determine the time evolution of the solute distribution within the fluid layer using two different estimates of the solute distributions immediately after filling. One is the step distribution assuming perfect filling; the other is a three-equal-layer distribution, with the top and the bottom layers at 2.0 wt % and 0.0 wt % ethanol–water solutions and the middle layer with a linearly varying distribution to account for the mixing effect. The predicted solute distributions resulting from these two different initial conditions are nearly equal to each other. Quantitatively, the relative error of the predicted values of ΔS based on the two initial conditions is within 5 % at 90 min after the start of the experiment. Since the three-layer initial condition takes into account the mixing effect, we use it to predict the solute distribution in the tank up to the time of onset of instabilities. The solute distributions at $t = 0$, 86 min and 95 min into the experiment are shown in figure 1. In the experiments,

Steady gravity				
Exp	$\Delta T\,\mathrm{K}^{-1}$	Ra_T	$t_{onset}\ \mathrm{min}^{-1}$	
H1	10.24	163 080	99.0	
H2	10.16	161 540	98.0	
H3	10.17	161 770	92.0	
H4	10.08	160 310	90.0	
H5	10.12	160 910	91.0	
H6	10.17	161 770	99.0	
Avg	10.16	161 560	94.8	
Gravity modulation				
Exp	$\Delta T\,\mathrm{K}^{-1}$	Ra_T	$t_{onset}\ \mathrm{min}^{-1}$	
H7	10.24	162 790	90.0	
H8	10.21	162 360	87.0	
H9	10.27	163 230	91.0	
H10	10.07	160 170	82.0	
H11	10.08	160 310	81.0	
H12	10.13	161 040	87.0	
H13	10.02	159 290	82.0	
Avg	10.15	161 330	85.7	
Experimental onset characteristics				
	Ra_T	Ra_S	f_{onset}(Hz)	λ
Steady gravity	161 560	125 540	0.043	0.82–1.06H
Gravity modulation	161 330	136 140	0.057	1.39–2.26H

TABLE 1. Experimental conditions and results.

instability onset was observed at 80–100 min. The buoyancy frequency estimated for the stratification at $t = 0$ is 0.37 Hz based on the solute gradient in the mid-section of the fluid layer. Thereafter, the image of the illuminated particles in the fluid layer displayed on the computer screen is monitored for onset of instability and subsequent motion. For experiments with gravity modulation, the oscillating platform is activated at the same time as ΔT is imposed.

3. Experimental results

3.1. *Steady gravity*

Six experiments were carried out under steady gravity. The test conditions and results in terms of the ΔT across the tank, the time of instability onset, and the Rayleigh numbers Ra_T and Ra_S corresponding to the mean time of onset are given in table 1. The average value of Ra_T is 161560 with variations of $\pm 1.0\,\%$, and the mean onset time is 94.8 min $\pm$ 5.0 %. Based on the solute difference ΔS at 94.8 min as computed by the diffusion equation, the critical $Ra_S = 125\ 540 \pm 3.5\,\%$.

The time of instability onset is first determined approximately by noticing the onset of motion of the particles in the fluid layer as recorded in the flow-visualization movie. Then the recorded movie frames during that time period are processed by the PIV program to find the vertical velocity component at a point. Such data obtained for experiment H5 are shown in figure 2 for a 5 min period. The time when the random oscillations of the vertical velocity are changed to a growing oscillation of constant frequency is defined as the time of instability onset. For this case, the onset time is 91 min after the initial state.

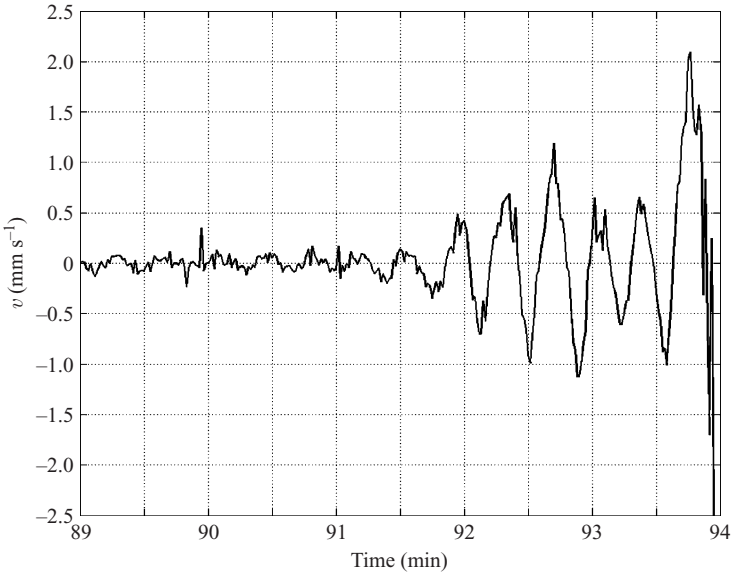

FIGURE 2. Vertical velocity at a point in experiment H5 under steady gravity. Instability onset is at 91 min.

The instability onset process is illustrated by streakline images taken from experiment H6, for which the critical time of onset of instability is at 99 min. A sequence of ten streakline images from 98 to 109 min is shown in figure 3. These images show the central 5 cm section of the test tank. The time interval between images is 1 min, except for images 8, 9 and 10, where the interval is 2 min. The exposure time is 6 s for images 1 and 2, and 4 s for all others. There is no motion in image 1, but in image 2, fluid motion in the form of five vortices can be clearly seen in the lower half of the tank. One minute later, image 3, vortices now appear in the upper half of the tank, rotating at lower speeds than those in the lower half, and there are more vortices in the lower half. Onset of instabilities is expected to occur near the two horizontal boundaries because of the lower solute gradient near the non-diffusive boundaries. However, because of the variable viscosity of the fluid, the higher local thermal Rayleigh number near the warmer lower boundary causes earlier onset of the instability in the lower part of the tank. These vortices are the result of double-diffusive instability rather than the result of Rayleigh–Bénard instability in the two nearly constant solute layers adjacent to the horizontal boundaries. In the latter case, the thickness of each of these layers must be $\geqslant 0.33$ cm. Solute stratification in these layers of such thickness cannot be ignored (figure 1). At 102 min, image 5, two rows of vortices fill the entire 5 cm section of the tank with wavelength $\lambda = (0.91\text{–}1.09)H$. Then the vortices grow bigger as seen in image 6, while some of the stacked vortices at the left-hand end start to merge into one large cell. This merging process continues until 109 min, image 10, when the solute gradient vanishes owing to mixing and the flow pattern becomes that of Rayleigh–Bénard convection.

For a stably stratified fluid with heating from below, the instability is in the oscillatory mode when Ra_S exceeds a value based on the Prandtl and Lewis numbers of the fluid. For the present test fluid, the limiting $Ra_S \approx 0.1$. Since the experimental $Ra_S \approx 120\,000$, oscillatory onset is expected. For the present case, each of the vortices shown in figure 3 is in oscillatory motion that is consisted of an oscillatory rotation

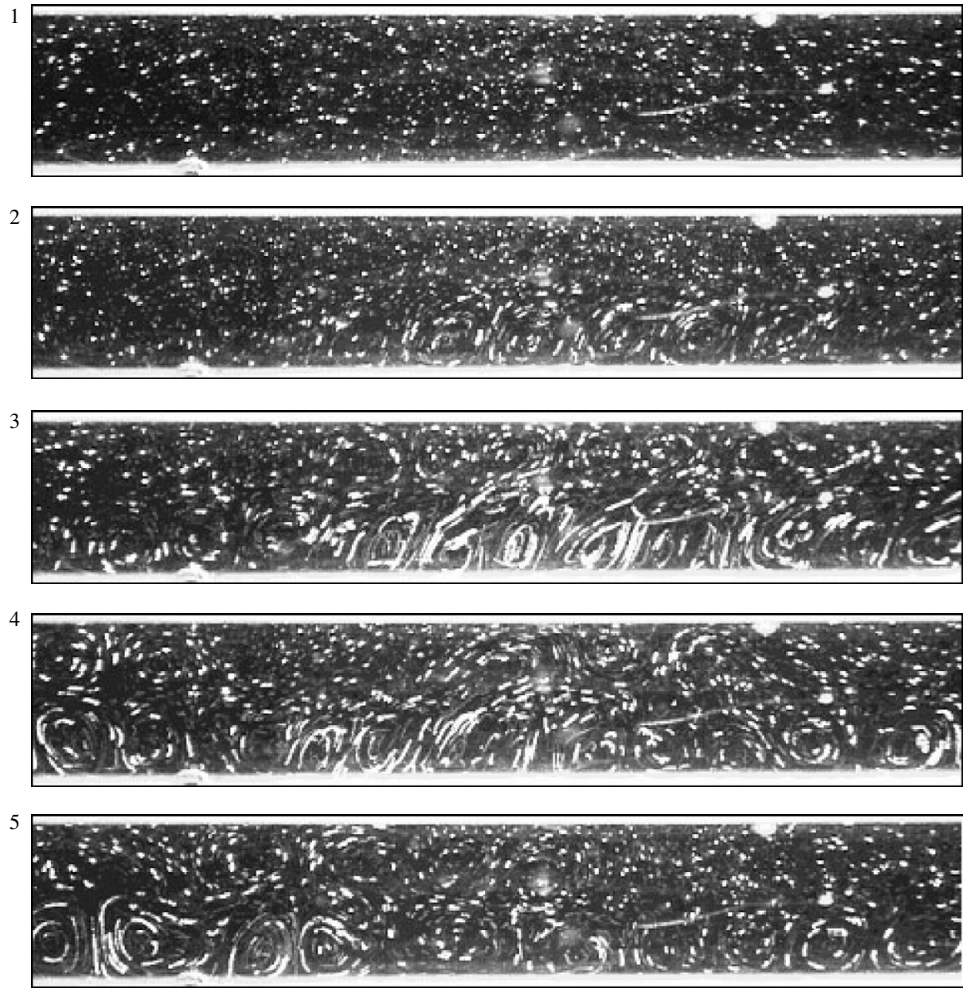

FIGURE 3. For caption see next page.

and, to a lesser extent, a lateral translation of the vortex as a whole. This can be clearly seen in figure 4, in which the velocity vectors are shown in 5 s intervals starting at the second image (99 min) of figure 3 for 25 s, approximately one period. The vortex just to the right of the 10 mm mark, for instance, starts out with clockwise rotation, slows down and assumes counterclockwise rotation in images 3 and 4 (10–15 s), and then switches back to clockwise rotation in image 6 at 25 s. At the same time, there is a slight left–right oscillation of the vortices as a whole. The results of numerical simulations in § 5, however, show only rotational oscillation of each individual vortex without any lateral oscillations.

In order to obtain a quantitative measure of the frequency of the oscillatory nature of the flow field, we estimate the power spectrum of the time sequence of the vertical component of the velocity. The time sequence is obtained by analysing the experimental images using the PIV program. The sequence is usually ∼5–10 min long and is sampled every second. Taking the time sequence as a discrete-time signal, we estimate its power spectrum using the periodogram, the modified covariance method, and Burg's method; see Hayes (1996) and Proakis & Manolakis (1996). The dominant

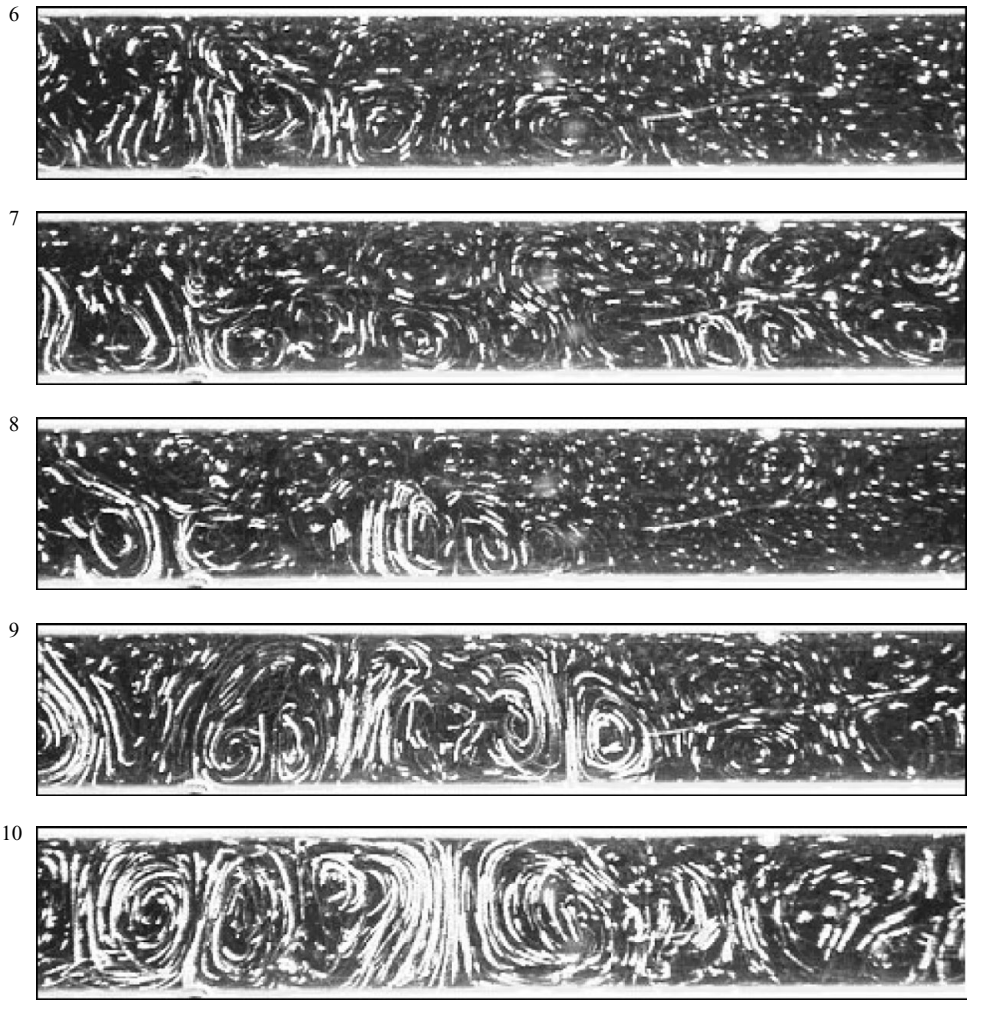

FIGURE 3. Sequence of streakline images showing the onset process in experiment H6 under steady gravity. Image 1 is at 98 min; subsequent images are shown at 1 min intervals except for the last two images which are shown at 2 min intervals. Exposure time is 6 s for images 1 and 2, and 4 s for all the rest.

frequency is determined according to the overall behaviour of the power spectra from the three estimations (figure 5). A frequency is considered as the dominant frequency when at least two of the three methods yield the same frequency.

This procedure is applied to time sequences of the vertical velocities at 70 discrete points in the tank, which spanned the range of $x = (0.25\text{–}0.75)W$ and $y = 0.25H$ in each experiment. These sampling points are schematically shown in figure 6. In the same figure, we also locate the three sampling points (indicated by $+$) for the simulation results to be discussed in § 5. The results obtained from all sampling points where instability has occurred for all six experiments are summarized in figure 7 in which the dominant frequency of the instability motion f_{onset} is shown. The statistical distribution of the frequencies is shown in figure 8, together with the Gaussian distribution curve. From this result, we determine $f_{onset} = 0.043$ Hz. For a double-diffusive fluid layer with linear temperature and solute profiles and

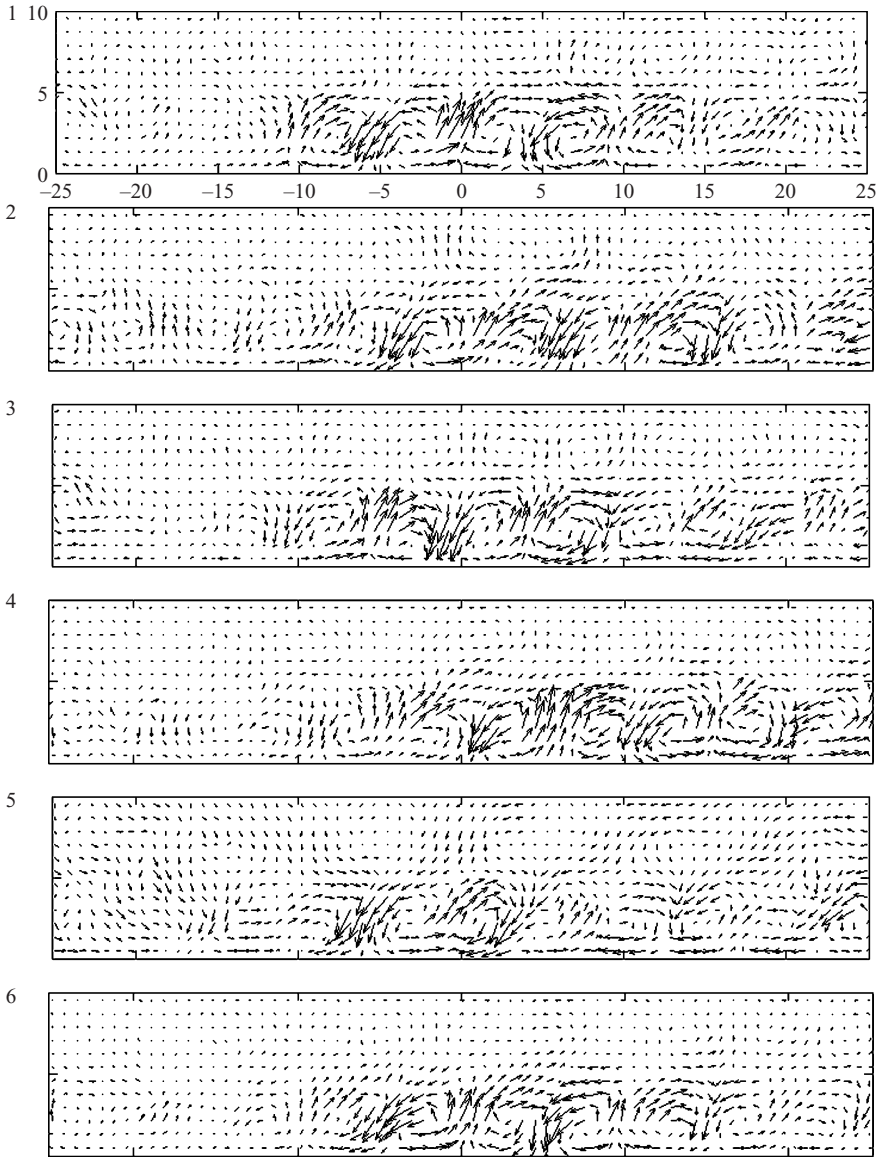

FIGURE 4. Velocity vectors at 5 s intervals starting at image 2 of figure 3 showing the oscillatory motion of the vortices under steady gravity. Length scale in millimetres.

free dynamic boundaries, the onset frequency predicted by linear stability theory is $[(1 - Le^{-1})/3(Pr + 1)]^{1/2}N$, where N is the buoyancy frequency (Turner 1973). Using the ΔS value at the time of onset, the predicted frequency is 0.053 Hz, indicating that the solute gradient in which the instability is occurring is lower than the mean solute gradient in the tank.

3.2. *Gravity modulation*

Before the experiments under gravity modulation are carried out, we first measure the gravity variations actually experienced by the oscillating platform. The accelerometer data of the cyclic motion are shown in figure 9. Because of a slight asymmetry in the

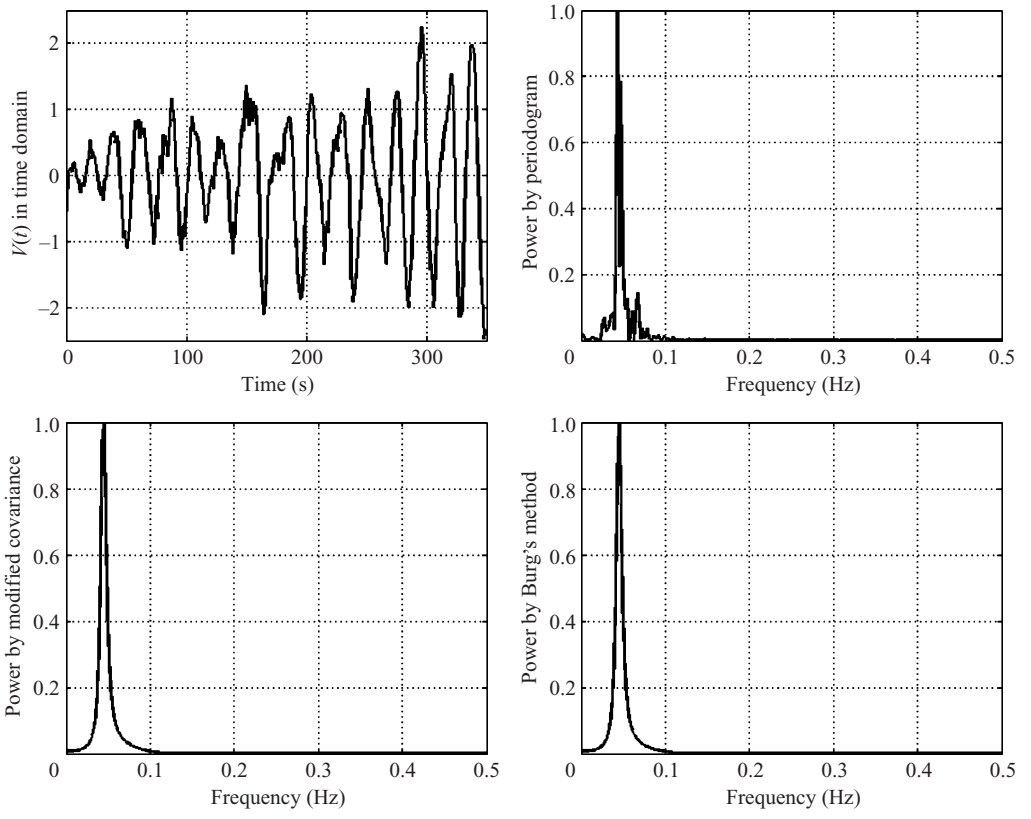

FIGURE 5. Power spectrum estimates by three different methods of a sample time sequence of the vertical velocity taken from experiment H2.

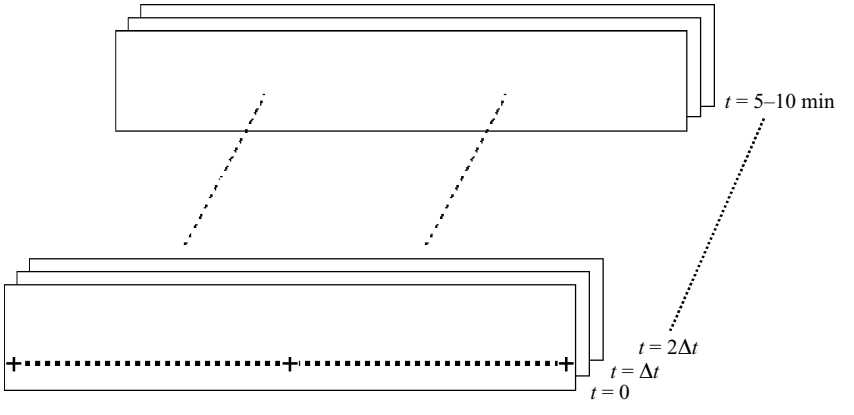

FIGURE 6. Schematic representation of velocity sampling points for the experiments (■) and for the numerical simulations (+).

harmonic motion of the platform, the acceleration of the platform shows noticeable irregularity. In addition to the asymmetry, now much exaggerated, there is a ripple in the acceleration at the apex of the down-stroke owing to the backlash in the speed-reduction gearing of the d.c. motor. The effect of these deviations from the

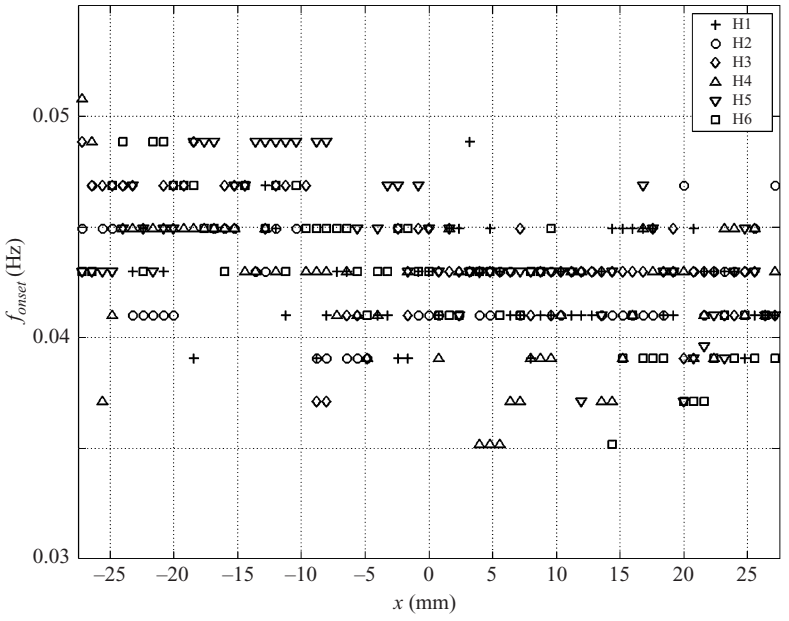

FIGURE 7. Dominant frequencies from all six experiments under steady gravity.

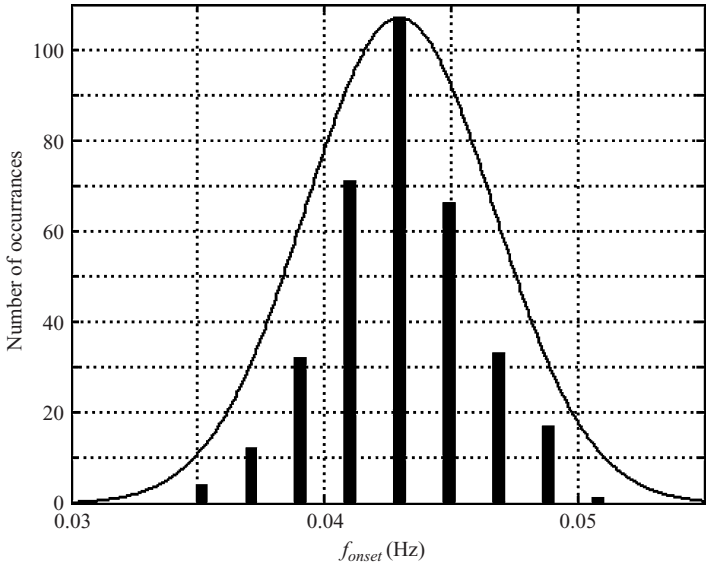

FIGURE 8. Statistical distribution of the dominant frequencies from all six experiments under steady gravity.

ideal sinusoidal variations of the acceleration will be examined in our numerical simulations.

Seven experiments were conducted with gravity modulation and the results are also summarized in table 1. With essentially the same Ra_T as in the steady gravity case, the average time for instability onset is 85.7 min $\pm$ 5 %, resulting in a higher average $Ra_S = 136\,140$, an 8.4 % increase from the steady gravity case. The fluid layer is destabilized by gravity modulation.

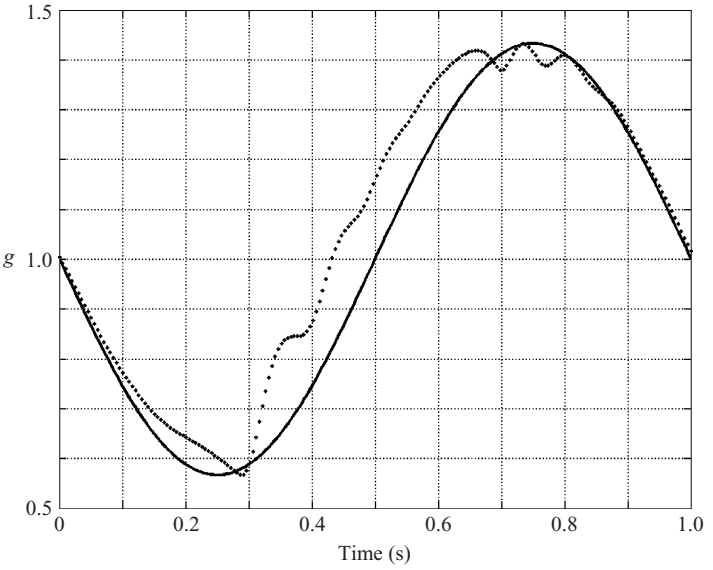

FIGURE 9. Gravity variations as experienced by the oscillating platform. Measured values shown in dotted line; ideal modulation shown in solid line.

There are also differences in the fluid motion after the onset of instabilities. Among the seven experiments conducted, the streakline images from two of them show the two-layer cellular structure at onset similar to those in experiments under steady gravity; but in this case, the convection cells are elliptical with wavelength $\lambda = (1.4 - 1.9)H$. Also, they evolve into the one-layer structure in a shorter time than in the steady gravity case. In the other five experiments, the onset motion is in large vortices that span the entire height of the tank. This is illustrated in a sequence of 10 streakline images starting at 86 min and ending at 95 min from experiment H8 shown in figure 10. The time interval between images is 1 min; the exposure time is 6 s for images 1 and 2, and 4 s for the rest. Motion started at the second image, 87 min, in a large vortex near the right-hand end. More and more vortices are formed, and by image 5, the entire 5 cm span is filled with five vortices. Thereafter, there is merging among the cells in the mid-section of the tank. The measured wavelength at onset is $\lambda = (1.39 - 2.26)H$.

The oscillations of the cell rotation as well as the lateral oscillations of the cells are illustrated by the velocity vectors shown in figure 11. Starting with image 5 of figure 10, the velocity vectors are shown every 5 s for a total duration of 20 s, approximately one cycle of oscillation. For the gravity modulation case, the lateral oscillations are of larger amplitude than the steady gravity case. Looking at the pair of vortices at the right-hand end in image 1, the pair moves to the left $\sim$5 mm and keeps the same individual rotation at 5 s, image 2. At 10 s, image 3, they move back to their original position but with opposite rotation. At 15 s, image 4, the pair moves to the left again with no change in the rotation. Finally at 20 s, image 5, the pair returns to their original position and their original rotation.

Following the same procedure as in the steady gravity case, we obtain the most probable frequency of oscillation at the onset of instabilities by analysing the time sequence of the vertical velocity. We note here that the vertical velocity grows faster and oscillates at a higher frequency than that in the steady gravity case. The statistical

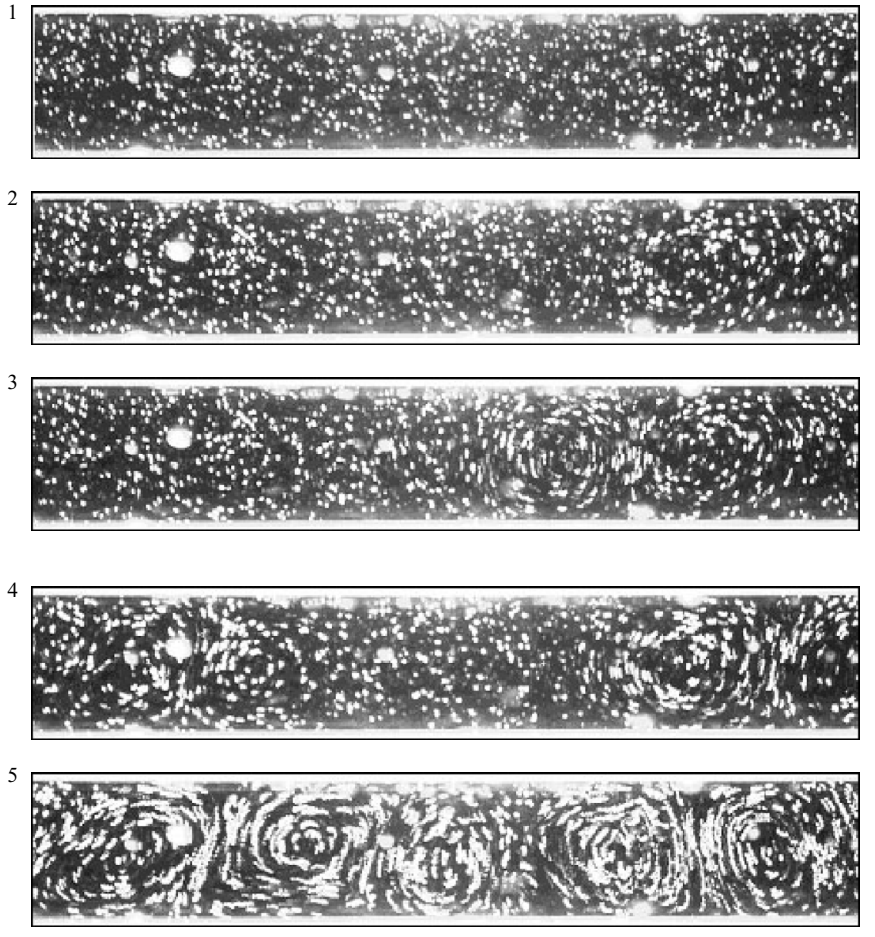

FIGURE 10. For caption see next page.

distribution of the frequency data obtained from all seven experiments is shown in figure 12. The distribution curve is much broader than the steady gravity case and the most probable value is $f_{onset} = 0.057$ Hz, a 32.6 % increase from the steady gravity case. There is a small peak at the most probable f_{onset} for the steady gravity case.

4. Linear stability theory results

The linear stability analysis is applied to study the effect of gravity modulation on the stability of a horizontal double-diffusive layer. The layer is confined within two rigid boundaries with constant stable solute gradient and unstable temperature gradient. The spectral-Galerkin method is used to transform the linear perturbation equations into a system of time-periodic ordinary differential equations. The Chebyshev expansion method of Sinha & Wu (1991) is applied to obtain the Floquet transition matrix. This method has been successfully used by Chen & Chen (1999) to study the effect of gravity modulation on thermal convection in a vertical slot.

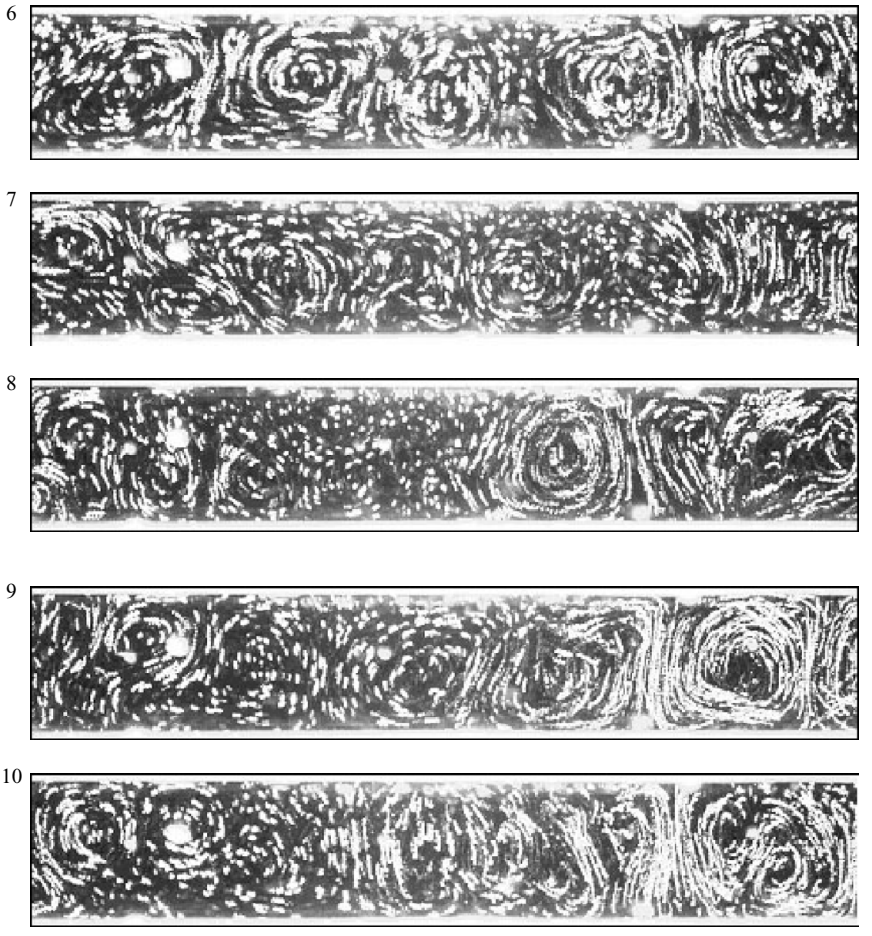

FIGURE 10. Sequence of streakline images showing the onset process in experiment H8 under gravity modulation. Image 1 is at 86 min; all subsequent images are shown at 1 min intervals. Exposure time is 6 s for images 1 and 2, and 4 s for all the rest.

In order to obtain quantitative predictions to compare with experimental results, the same methodology is applied for an initial sinusoidal solute distribution

$$S = S_0 - (\Delta S/2)\sin[\pi(y/H - 12)] \quad \text{for } 0 \leqslant y \leqslant H.$$

This expression gives a good approximation of the nonlinear solute distribution due to non-diffusive boundary conditions at the top and the bottom of the tank (see Tanny, Chen & Chen 1995). The value of ΔS is chosen to fit the S-distribution in the tank at instability onset. In figure 13, we show the marginal stability curves for a layer with linear and sinusoidal solute distributions at the same $Ra_S = 126\,000$. The same results apply to steady gravity and modulated gravity at 1 Hz with amplitude $0.41g$. Saunders *et al.* (1992) have shown that under gravity modulation at low frequency and large amplitude, there are resonant instability bands. However, under the present experimental gravity modulation conditions, linear stability theory yields the same marginal stability conditions as those for steady gravity, but the instability onset consists of a complex conjugate pair. For the linear solute distribution, the critical thermal Ra_T is 116 200. For the sinusoidal S-distribution, it becomes more stable,

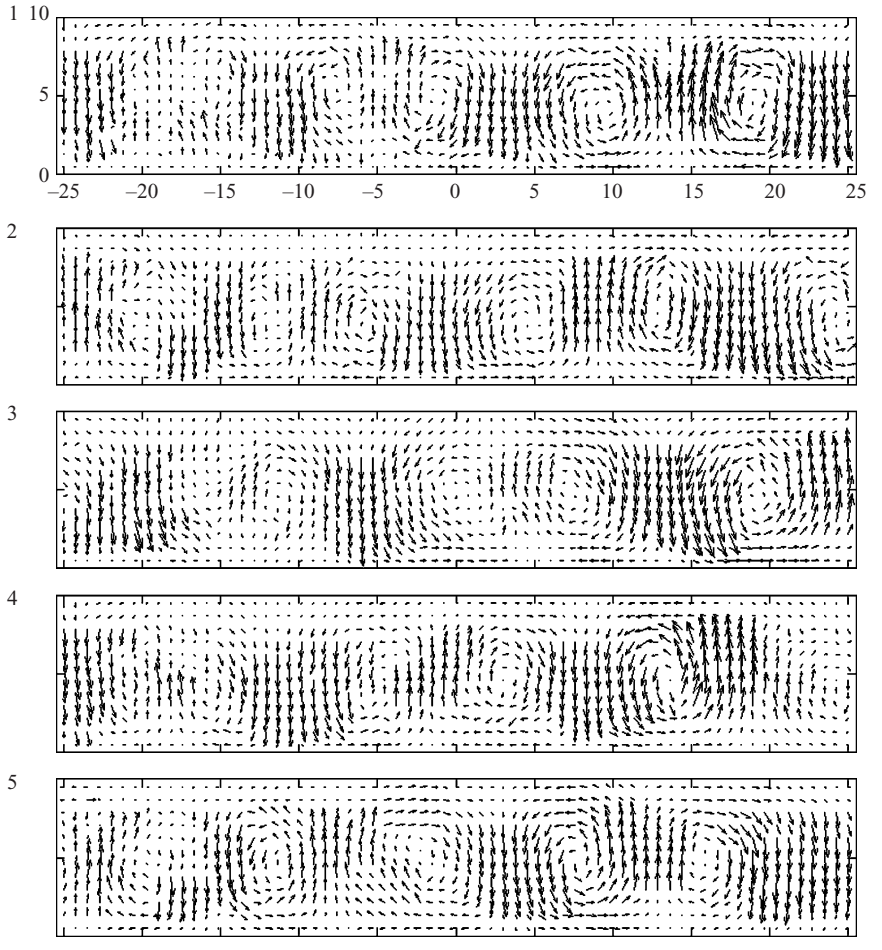

FIGURE 11. Velocity vectors at 5 s intervals starting at image 5 of figure 10 showing the oscillation of the vortices under gravity modulation. Length scale in millimetres.

with critical $Ra_T = 158\,000$, frequency of oscillation $f_{onset} = 0.045$ Hz, and critical wavenumber $k = 5.93$ under steady gravity. These results are summarized in table 2. The corresponding perturbation streamlines at onset show two rows of counter-rotating vortices all along the tank. These predictions agree very well with the experimental results under steady gravity. However, for the gravity modulation case, the linear stability theory predictions indicate the fluid layer is slightly more stable than the experimental results. The possibility of onset of subcritical instability is examined by numerical means in the next section.

5. Numerical simulations

Two-dimensional nonlinear simulations are carried out for the instability problem we studied in the experiments. It is assumed that a Newtonian fluid with variable viscosity is contained in a two-dimensional rectangular domain of width W and height H with aspect ratio $A = W/H = 11$. The temperatures of the top and bottom walls are kept at constant at T_t and $T_b(>T_t)$ while the sidewalls are held adiabatic. All walls are non-diffusive with respect to the solute. The origin of the x, y (horizontal-vertical)

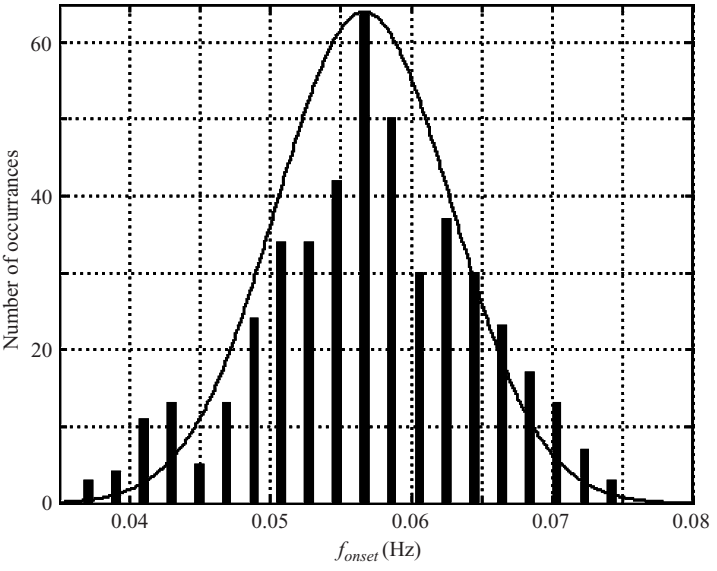

FIGURE 12. Statistical distribution of the dominant oscillation frequencies from all seven experiments under gravity oscillation.

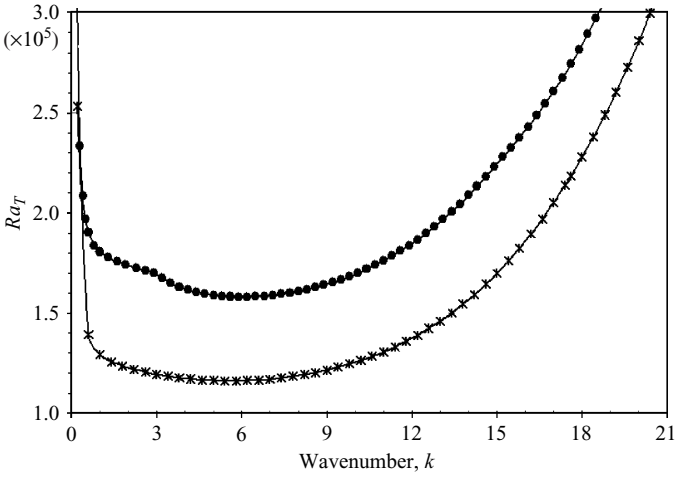

FIGURE 13. Marginal stability curves based on linear stability analysis: ●, sinusoidal profile; ×, linear profile.

coordinate system is at the lower left-hand corner of the tank (figure 14). The gravity vector points downward and its magnitude oscillates with non-dimensional amplitude g_1 and frequency Ω about a mean g:

$$\boldsymbol{g} = -\boldsymbol{j}\, g(1 + g_1 \cos\, \Omega t). \tag{1}$$

The fluid is assumed to be Bussinesq and its density is linear both in temperature and solute concentration, $\rho = \rho_0[1 - \beta_T(T - T_0) + \beta_s(S - S_0)]$. The non-dimensional equations of continuity, momentum, energy conservation and solute conservation

	Ra_T	Ra_S	f_{onset} (Hz)	λ
Linear stability analysis				
Steady gravity	158 000	126 000	28.29/0.045	1.06H
Gravity modulation	158 000	126 000	–	1.06H
Numerical Simulations				
Steady gravity	161 560	122 560	28.27/0.045	0.82–1.00H
Ideal gravity modulation	161 560	122 560	28.27/0.045	0.82–1.00H
Actual gravity modulation	161 560	124 330	30.66/0.049	0.82–1.00H

TABLE 2. Onset conditions based on linear stability analysis and numerical simulations.

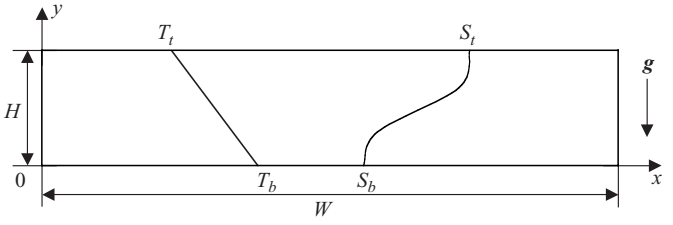

FIGURE 14. The coordinate system.

written in terms of streamfunction ψ and vorticity ξ are

$$\frac{\partial^2\psi}{A^2\partial x^2}+\frac{\partial^2\psi}{\partial y^2}=-\xi, \tag{2}$$

$$\begin{aligned}\frac{\partial\xi}{\partial t}=&\left(\frac{\partial\psi}{A\partial x}\frac{\partial\xi}{\partial y}-\frac{\partial\psi}{\partial y}\frac{\partial\xi}{A\partial x}\right)+f_v\left(\frac{\partial^2\xi}{A^2\partial x^2}+\frac{\partial^2\xi}{\partial y^2}\right)\\&+\frac{Ra_T}{Pr}\left(1+g_1\cos(\omega_m t)\right)\frac{\partial\theta}{A\partial x}-\frac{Ra_S}{Pr}\left(1+g_1\cos(\omega_m t)\right)\frac{\partial C}{A\partial x}\\&+2\left(\frac{\partial f_v}{A\partial x}\frac{\partial\xi}{A\partial x}+\frac{\partial f_v}{\partial y}\frac{\partial\xi}{A\partial y}\right)-\left(\frac{\partial^2 f_v}{A^2\partial x^2}-\frac{\partial^2 f_v}{\partial y^2}\right)\left(\frac{\partial^2\psi}{A^2\partial x^2}-\frac{\partial^2\psi}{\partial y^2}\right)\\&-4\frac{\partial^2 f_v}{A\partial x\partial y}\frac{\partial^2\psi}{A\partial x\partial y},\end{aligned} \tag{3}$$

$$\frac{\partial\theta}{\partial t}=\left(\frac{\partial\psi}{A\partial x}\frac{\partial\theta}{\partial y}-\frac{\partial\psi}{\partial y}\frac{\partial\theta}{A\partial x}\right)+\frac{1}{Pr}\left(\frac{\partial^2\theta}{A^2\partial x^2}+\frac{\partial^2\theta}{\partial y^2}\right), \tag{4}$$

$$\frac{\partial C}{\partial t}=\left(\frac{\partial\psi}{A\partial x}\frac{\partial C}{\partial y}-\frac{\partial\psi}{\partial y}\frac{\partial C}{A\partial x}\right)+\frac{1}{PrLe}\left(\frac{\partial^2 C}{A^2\partial x^2}+\frac{\partial^2 C}{\partial y^2}\right), \tag{5}$$

where $u=\partial\psi/\partial y$, $v=-\partial\psi/A\partial x$ and $\xi=\partial v/A\partial x-\partial u/\partial y$. The scaling quantities to render these equations non-dimensional are H for the vertical length, AH for the horizontal length, H^2/ν for time, and ν/H for velocity. For the gravity modulation term, ω_m is the non-dimensional modulation frequency. The non-dimensional temperature θ and solute concentration C are defined as $\theta=(T-T_0)/\Delta T$ and $C=(S-S_0)/\Delta S$, where $\Delta T=T_b-T_t$ the imposed temperature difference and $\Delta S=2\,\%$. T_0 is the mean of the boundary temperatures, and $S_0=1\,\%$. The kinematic viscosity ratio is approximated by $f_v(\theta)=1-0.24888\theta$, which corresponds to the viscosity variation due to the actual temperature difference in experiments.

The boundary conditions are

$$\psi = \frac{\partial \psi}{\partial x} = 0, \quad \frac{\partial \theta}{\partial x} = 0, \quad \frac{\partial C}{\partial x} = 0 \quad \text{at } x = 0, 1, \tag{6}$$

$$\psi = \frac{\partial \psi}{\partial y} = 0, \quad \theta = 0.5, -0.5, \quad \frac{\partial C}{\partial y} = 0 \quad \text{at } y = 0, 1. \tag{7}$$

The initial conditions are the quiescent state at the uniform $\theta = 0.0$ and the solutal distribution at $t = 0$ as shown in figure 1. In our notation, positive Ra_T is destabilizing whereas positive Ra_S is stabilizing.

For a better understanding of the energetics during the period of instability onset, we calculate the substantial derivative of the kinetic energy of the fluid particle by forming the inner product of the velocity with the momentum equation. For simplicity, only the case of constant viscosity is considered. The time rate of change of the kinetic energy at any point in the flow field is

$$\frac{\mathrm{D}}{\mathrm{D}t}\left(\frac{u^2 + v^2}{2}\right) = -\left(u\frac{\partial p}{A\partial x} + v\frac{\partial p}{\partial y}\right) + (u\nabla^2 u + v\nabla^2 v) + v\frac{Ra_T}{Pr}\theta - v\frac{Ra_S}{Pr}C, \tag{8}$$

in which the four terms on the right-hand side are the pressure work, the shear work, the thermal buoyancy work and the solutal buoyancy work, respectively.

For the numerical solution of the equations above, the time derivatives are discretized by the central-difference method, the convection terms by the Arakawa (1966) nine-point method, the diffusion terms by the DuFort–Frankel method (DuFort & Frankel 1953), and the Poisson equation, (2), by a fast Fourier solution technique using the fourth-order-accurate nine-point finite-difference scheme of Houstis & Papatheodorou (1979). The boundary vorticity is determined by Thom's rule (Roache 1982) which has been shown to be second-order accurate by Huang & Wetton (1996) and Napolitano, Pascazio & Quartapelle (1999). The kinetic energy expression, equation (8), and the extra terms due to variable viscosity in (3) are discretized by central-difference approximation. The overall scheme is temporally and spatially second-order accurate. A detailed validation of the code based on this scheme is presented in Chan, Yu & Chen (2004) for a thermal convection problem in a vertical tank. It is further validated by applying this code to a double-diffusive problem considered by Ghorayeb & Mojatabi (1997). They studied the onset of double-diffusive convection in a vertical tank with equal and opposite buoyancy forces due to horizontal thermal and solute gradients. For a square cavity, they found by direct numerical simulation that subcritical convection begins when the Rayleigh number $Ra \geqslant 676$ for a fluid with $Pr = 1$ and $Le = 11$. Using the current method with 33×33 grid points, the onset Rayleigh number is between 679.5 and 679.7. When the grid points are increased to 65×65, the critical Rayleigh number is between 675.99 and 676.00.

For our numerical simulations, computations are usually run with $513(x) \times 65(y)$ grid points and time step $\Delta t = 0.0001$, with continuous random perturbations of magnitude 5×10^{-6} superposed on the flow variables. This grid size is optimal for achieving a convergent solution and yet affordable computation time. The numerical stability criteria (Courant–Friedrichs–Lewy conditions) are checked at every time step to eliminate artificial numerical oscillations. The fluid layer is considered stable if there is no increase in $|\psi|$ when calculations are carried out to $t = 250$. The random perturbation is generated by a built-in function, which uses the Prime Modulus M Multipicative Linear Congruential Generator. The seed is set based on time. For the steady gravity case, we have experimented with different ways of perturbing

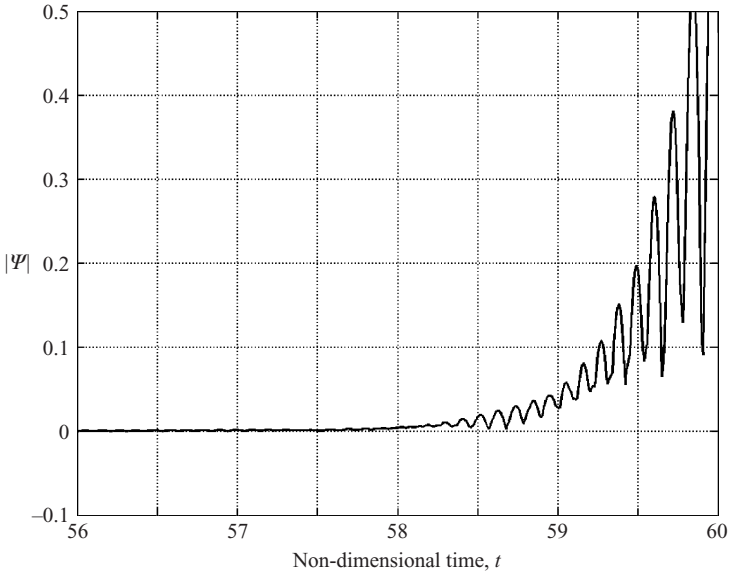

FIGURE 15. Time evolution of the streamfunction $|\psi|$ under steady gravity showing instability onset at $t = 58$.

the system: (i) perturbations on ψ, θ and C; (ii) perturbations on ξ, θ and C; and (iii) perturbations on ξ, ψ, θ and C with three different seeds or times. The predictions of the onset times are between 58.0 and 58.8. Within this error limit, it does not seem to matter which set of flow quantities are perturbed or which seed number is used. In the following, the computed results of instability onset and the subsequent nonlinear evolution to the final state of thermal convection for steady gravity, the ideal sinusoidal gravity modulation, and the actual experimental gravity modulation cases are presented. All these results were obtained with initial random perturbations assigned by method (iii) presented above with the same seed number.

5.1. *Steady gravity*

In numerical simulations, the time of onset of instability is defined as the time when $|\psi| \geqslant 0.01$. This is usually accompanied by the growth and onset of oscillations of $|\psi|$ and the first appearance of streamline contours in the flow field. The value of $|\psi|$ is the mean of the values at the three sampling points (2.75, 0.25), (5.5, 0.25) and (8.25, 0.25) shown in figure 6. The time of instability onset is not too sensitive to the exact value of the critical $|\psi|$. Had we selected the value to be 0.001, the onset time would be shortened by approximately 2 min resulting in a 1.6 % increase in the critical solute Rayleigh number. The experimental scatter is about 10 min. The time evolution of $|\psi|$ for the steady gravity case is shown in figure 15 in non-dimensional units. We note here that the non-dimensional time unit is 99.5 s. It can be seen that time of onset is $t = 58$ (=96.2 min). At this time, $|\psi|$ starts to grow from a near-zero value to oscillations of ever-increasing magnitudes. A sequence of 9 streamline images is shown in figure 16 to illustrate the onset process with image 1 at $t = 58$. Each of the subsequent images, except for image 9, are presented at 1 min intervals to facilitate comparison with the experimental streaklines shown in figure 3. For the last two images, the interval is 4 min. The streaklines in figure 3 are taken from flow-visualization data in the central 5 cm of the test tank. For image 1, $\Delta\psi = \pm 0.010$,

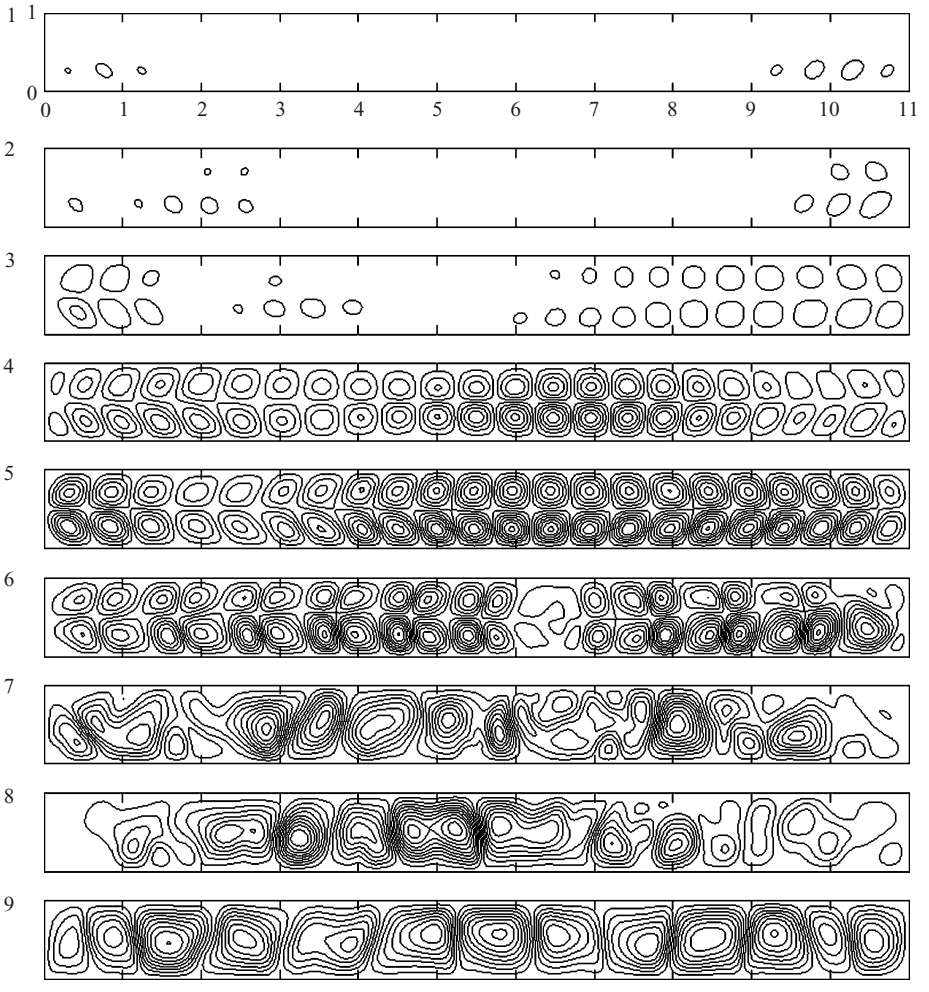

FIGURE 16. Sequence of streamline patterns illustrating the development of instability onset under steady gravity. Image 1 is at onset, $t = 58$ (96.2 min). The time interval between images is 1 min except for image 9 which is 4 min after image 8. Values of $\Delta\psi = \pm 0.01$ for images 1 to 4; ± 0.03 for image 5; ± 0.15 for image 6; ± 0.30 for image 7; ± 0.5 for image 8; ± 0.8 for image 9.

approximately 2×10^3 times the level of the random noise in the flow field. Similar to the experiment, the streamline images show that the onset of instability takes place first in the lower half of the tank owing to effect of variable viscosity. Cellular motion in the upper half of the tank can be seen 1 min later, and by the third minute the tank is filled with two rows of counter-rotating vortices with the stronger ones in the lower half. The simulation results show only oscillatory rotation of the convection cells, but no lateral oscillations. The merging of smaller vortices into larger ones occurs in image 6. The merging process continues, resulting in a row of nearly equal cells of Rayleigh–Bénard convection all along the tank in image 9, which is 11 min after the onset of instabilities. This process is generally similar to the experimental results shown by the streaklines in figure 3.

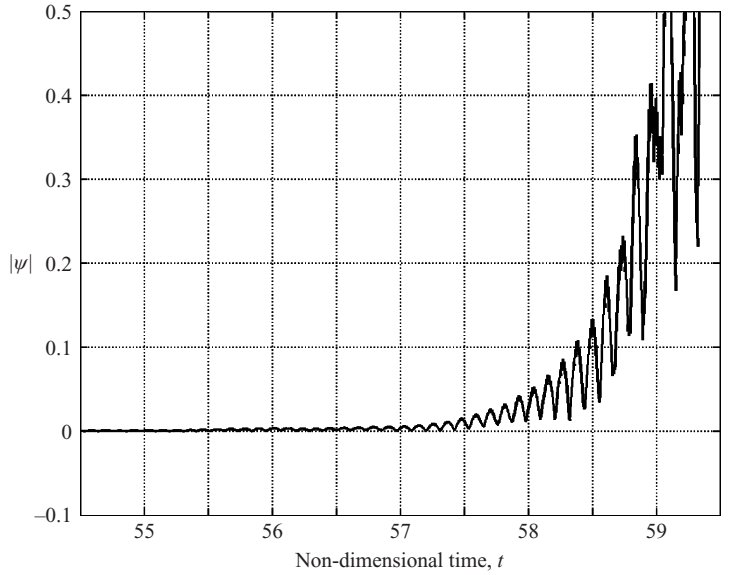

FIGURE 17. Time evolution of the streamfunction $|\psi|$ under actual gravity modulation showing instability onset at $t = 55.5$.

The critical wavelength is determined by the cells in images 3, 4 and 5 to be $\lambda = (0.82 - 1.00)H$, which agrees well with $(0.91 - 1.09)H$ found from the experiment. The solute Rayleigh number determined from the time of onset is $Ra_S = 122\,560$. The power spectrum of the vertical velocity at the three sampling points yields, as expected, a narrow distribution of frequencies from $(0.041 - 0.049)$ Hz, with the peak value at $f_{onset} = 0.045$ Hz, which compares well with the experimental value of 0.043 Hz. The onset characteristics, together with those from the ideal gravity modulation and the actual gravity modulation to be discussed below, are given in table 2.

5.2. *Ideal and actual gravity modulations*

For the simulations, we set the experimental values $g_1 = 0.41$ and $\omega_m = 628.3$ (=1 Hz). The results for the ideal gravity modulation show no discernible difference in the onset conditions from those for the steady gravity case. As shown in table 2, the critical solute Rayleigh number, the critical wavelength, and the frequency of oscillation at onset are all the same as those obtained for the steady gravity case. The simulation results are in agreement with the linear stability theory that sinusoidal oscillations at this high frequency do not affect the stability of the layer. However, in the nonlinear development of the flow, the merging of the initial two-cell structure into a single-cell structure is slightly accelerated over the steady gravity case.

For the actual gravity modulation case, we replace the sinusoidal gravity variations in the computations by the actual measured acceleration shown in figure 9. The time evolution of $|\psi|$ is shown in figure 17. The onset of instability is now advanced to $t = 55.5$ (=92.0 min). The corresponding critical solute Rayleigh number is 124 330, a 1.4 % increase from the steady-gravity case. The initial growth of $|\psi|$ is much slower than that in the steady-gravity case. Also, there are high-frequency oscillations in $|\psi|$ at the peak of each cycle, reflecting the ripple in the acceleration of the platform. The instability onset is always marked by the appearance of two rows of vortices. In no instance do we encounter the onset in terms of a row of large convection cells

spanning the entire height of the tank as seen in the experiments. The oscillation frequency at onset is 0.049 Hz, an increase of 8.9 % from the steady-gravity case. Despite the departure from the ideal gravity modulation, the subsequent nonlinear evolution is similar to the steady gravity and ideal modulation cases. From table 1, the experimental results show an 8.4 % increase for the critical solute Rayleigh number and a 32.6 % increase for the onset frequency between the steady- and modulated-gravity cases. In a two-dimensional flow, the non-symmetrical gravity-modulation effect cannot explain the differences in the changes observed in the experiments. This leads us to conjecture that the convective flow in the gravity-modulation case may be three-dimensional.

To check on such possibilities, we evaluate the relative error $[|\partial u/\partial x + \partial v/\partial y|/\{|\partial u/\partial x| + |\partial v/\partial y|\}]$ from the experimental velocity measurements at 980 locations evenly distributed in the image area at 4 min after instability onset in experiments H6 (steady gravity) and H8 (modulated gravity). These values were averaged to obtain a space-averaged error. Four more such averages were obtained at four subsequent times 5 s apart. The five space-averaged values vary between 0.553 and 0.580 for the steady-gravity case, and between 0.566 and 0.612 for the modulated-gravity case. These results indicate that the motion in the fluid layer after onset is three-dimensional for both cases. The difference in the results of simulation and experiment cannot be explained by this conjecture.

5.3. *Subcritical instability for the ideal gravity-modulation case*

The results of nonlinear analysis of double-diffusive convection by Huppert & Moore (1976) suggest that as the Lewis number is increased, there is the possibility of subcritical onset of instability in the steady convection mode. We have examined the possibility of such subcritical instability in an infinite horizontal fluid layer with the same stable sinusoidal solute distribution as that considered in § 4 with heating from below under ideal gravity modulation. The nonlinear instability analysis is done by simulating the evolution of the finite perturbation flow variables (ψ_1, ω_1, T_1, C_1) from the basic solution. Computations are carried out for a unit cell whose width is the critical wavelength. Periodical boundary conditions are applied in the horizontal direction to simulate the infinite layer. The critical thermal Rayleigh number for instability onset is found to be 157 885, essentially the same value as the linear stability result for steady and ideally modulated gravity. Starting with the onset condition, computations are made at thermal Rayleigh numbers lower than the critical, no convective state is found.

6. Energy considerations

6.1. *Steady gravity*

We examine the time rate of change of the total kinetic energy, the summation of all values in the tank, in the instability onset process. In these calculations, the fluid is assumed to be of constant viscosity to avoid excessive computation time. The results for the steady-gravity case are presented in figure 18 in which the kinetic energy term and all the work components are shown for a 2 min period from the time of instability onset at $t = 58.2$ (97 min). The magnitude of the pressure work term is very small and is magnified ten times in the graph for a clearer view. It can be seen that all terms are growing in an oscillatory mode after instability onset. As the convective motion moves a parcel of fluid upward (downward) imparting positive (negative) thermal buoyancy work, a concomitant negative (positive) solute

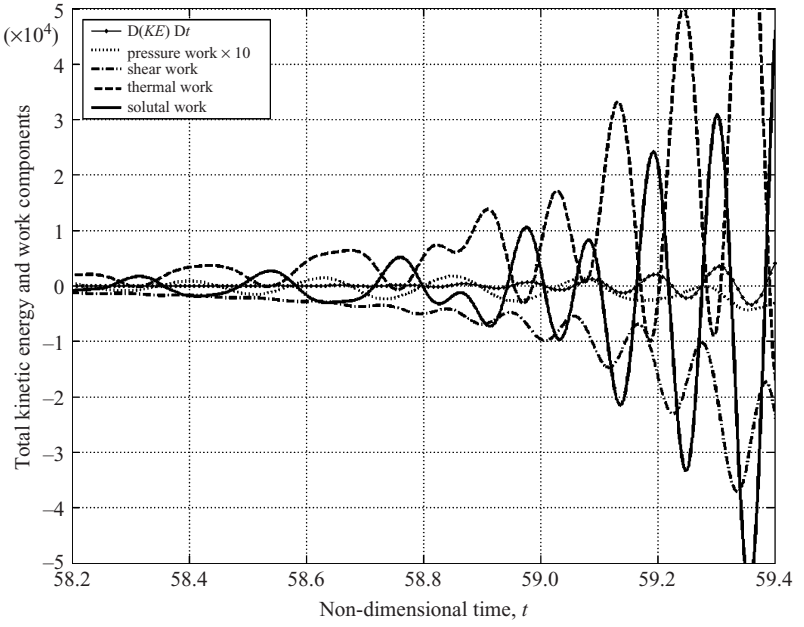

FIGURE 18. Oscillatory growth of the work components contributing to the time rate of change of kinetic energy at instability onset under steady gravity. Pressure work is amplified by a factor of 10 for a clearer view.

buoyancy work is generated. As a result, the thermal buoyancy work is exactly out of phase with the solute buoyancy work. The sum of the buoyancy work terms is mostly dissipated by the shear work, with a small remainder that is responsible for the gradual increase in the magnitude of $\mathrm{D}(KE)/\mathrm{D}t$. It is expected that all these terms should exhibit oscillations at twice the frequency of the instabilities at onset since they are all products of perturbation quantities. Power spectrum estimations show that, after $t = 59$, approximately 1 min after instability onset, all terms are oscillating at 0.090 Hz, twice the value of $f_{onset} = 0.045$ Hz. However, the thermal and solutal buoyancy terms oscillate initially at 0.044 Hz, but increase to twice the value at 0.090 Hz after $t = 59$, while the kinetic energy and the shear work oscillate at 0.090 Hz for all times from the onset of instabilities. It shows that there is a time lag of approximately 1 min for both θ and C from their respective diffusive states, resulting in the delayed response in frequency doubling.

In order to follow the evolution of these energy terms developing into the final thermal convection state, we extend the same plot to $t = 69$ ($\sim$15 min) in figure 19. The range of the ordinate is expanded to $\pm 6 \times 10^8$ to accommodate the explosive growth of the work terms. To make the graph easier to read, the $\mathrm{D}(KE)/\mathrm{D}t$ (pressure work) is shifted upward (downward) by 2×10^8. It can be seen that all energy terms start their rapid growth at $t \sim 60$, approximately 3 min after instability onset. After $t = 63$ ($\sim$105 min), thermal buoyancy work and the shear work predominate; thermal buoyancy drives the motion that is dissipated by shear. The solute buoyancy term reduces essentially to zero at $t = 64$ ($\sim$107 min), when the fluid becomes well mixed. The kinetic energy term oscillates about zero, and there is no net increase in the mean.

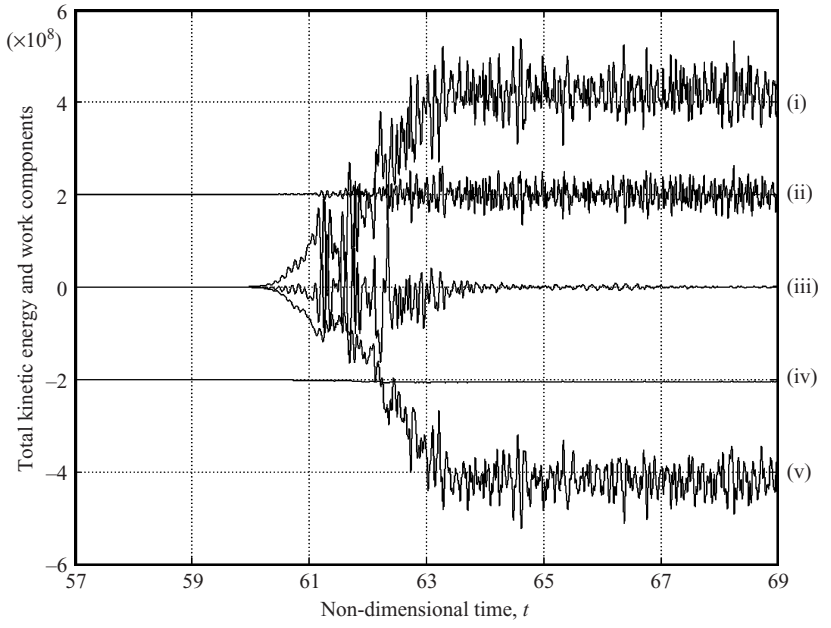

FIGURE 19. Development of all the energy terms into the final thermal convection state under steady gravity. For clearer presentation, the kinetic energy (pressure work) term is displaced upward (downward) by 2×10^8. (i) Thermal work; (ii) $\mathrm{D}(KE)/\mathrm{D}t$; (iii) solutal work; (iv) pressure work; (v) shear work.

6.2. *Ideal gravity modulation*

When the fluid layer is under gravity modulation, the pressure work term plays a more important role than in the steady-gravity case. The results of the calculation with ideal gravity modulation are shown in figure 20(*a*), with the effect of gravity modulation clearly shown. A small-magnitude oscillation at the modulation frequency is superposed onto all the growth curves of the work terms. The growth of the buoyancy and shear work terms is similar to the steady gravity case. However, the pressure work term, which is generated by the unsteady motion, is oscillating at the modulation frequency, with the magnitude growing within an envelop that is oscillating at twice the onset frequency. In fact, it is the major contributor to the $\mathrm{D}(KE)/\mathrm{D}t$ term. This remains the case when the flow is in the fully thermal convection state at $66 \leqslant t \leqslant 66.6$ (figure 20*b*). Now the solutal work is essentially zero, and all terms are oscillating at the modulation frequency. The thermal buoyancy work is dissipated by shear work; pressure work is sustaining the changes in the kinetic energy.

7. Internal wave mode of instability

Since our experiments were designed to be stable with respect to the internal wave instability, we explore the possibility of the onset of such instability using our simulation code. First, we consider the same solute-stratified fluid as in the experimental case under ideal gravity modulation without any heating. Then, we impose heating from below to study the possible interactions between the internal wave mode of instability and the double-diffusive instability.

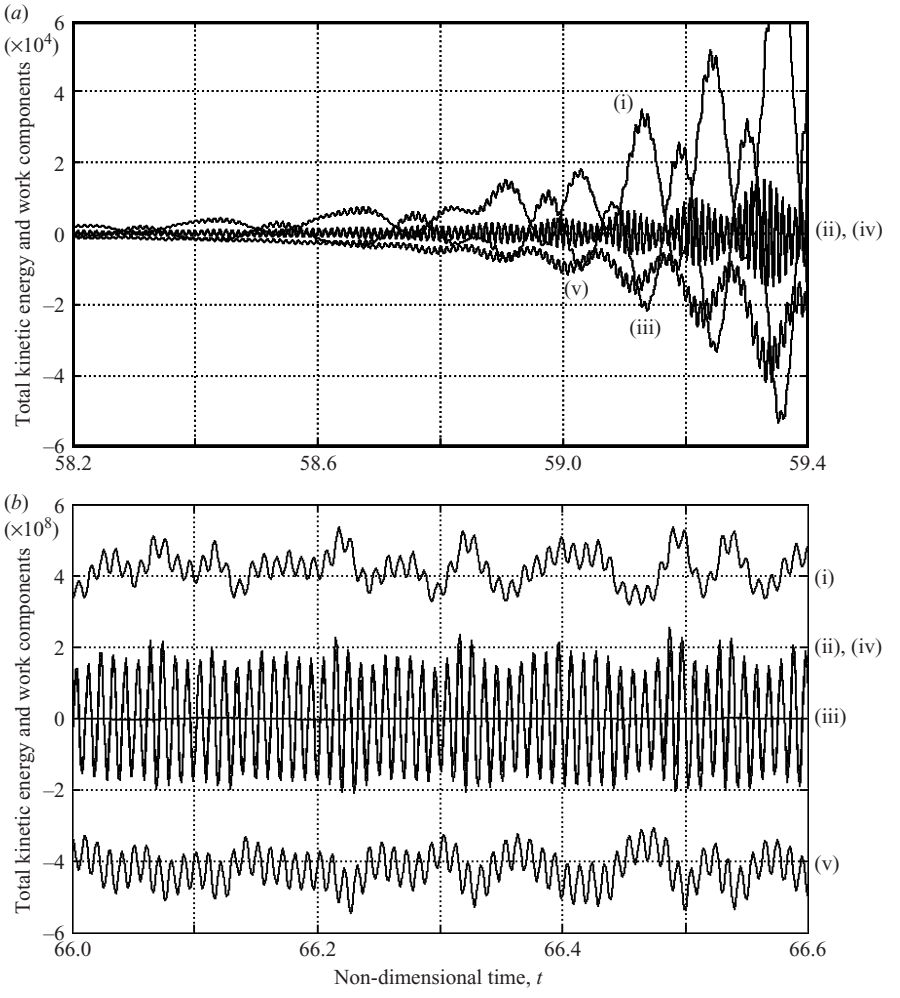

FIGURE 20. Growth of the work components contributing to the time rate of change of kinetic energy at (*a*) instability onset, and (*b*) final thermal convection state under ideal gravity modulation. (i) to (v) are the same as in figure 19.

7.1. *Solute-stratified layer*

We first set the modulation magnitude to be $g_1 = 0.41$, the experimental value, and carry out computations over a range of frequencies starting at $\omega_m = 0$. No instability is found up to $\omega_m = 628.3$ (1 Hz). When the modulation magnitude is increased to $g_1 = 0.75$, internal wave instability is found over a range of frequencies up to $\sim 2N$. The results are presented in figure 21(*a*), showing an instability island in the frequency range $220 \leqslant \omega_m \leqslant 430$ (0.35–0.68 Hz). Within this frequency range, instability onset occurs almost immediately after gravity modulation is imposed. The fluid motion is oscillatory in the subharmonic mode, and its magnitude grows with time. Since the solute gradient is being continuously eroded by diffusion enhanced by the oscillatory motion, the magnitude of the instability motion attains a maximum value and then starts to decrease. Eventually, the gradient becomes too small to sustain the instability motion and the layer becomes stable. In the critical frequency range, the time interval within which instability exists decreases with increasing modulation frequency. We

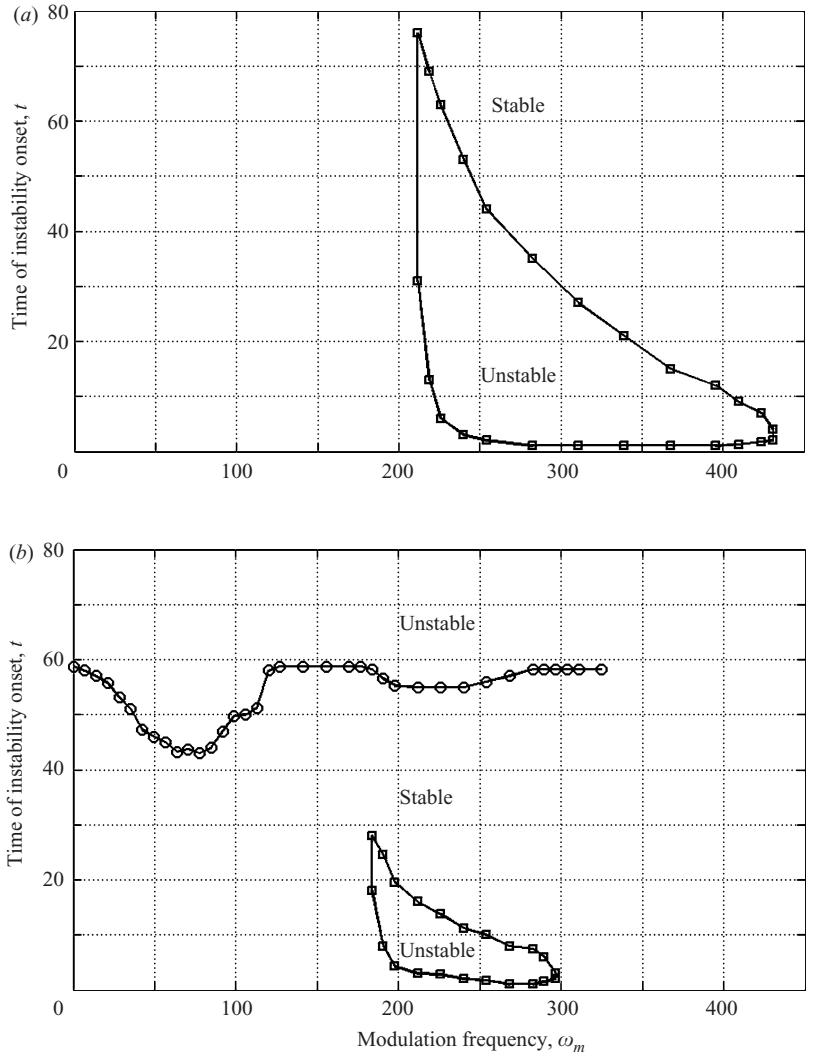

FIGURE 21. (*a*) Stability characteristics of a fluid layer with a stable solute distribution of the initial state under ideal gravity modulation with $g_1 = 0.75$ showing an island of internal wave instability. (*b*) The same layer with heating from below, $Ra_T = 161\,560$, showing the interaction between internal wave and double-diffusive instabilities at $180 \leqslant \omega_m \leqslant 300$, and the resonant instability of the double-diffusive layer at $\omega_m \leqslant 120$; □, internal wave; ○, double-diffusive instability.

note here that after the fluid layer regains stability, the mean solute gradient of the fluid is lower than an undisturbed layer at the same time. This type of instability is similar to those demonstrated by Gershuni *et al.* (1970) and Gresho & Sani (1970) for a fluid layer heated from above under gravity modulation.

7.2. *Solute-stratified layer with heating from below*

Now we subject the solute-stratified layer to an adverse temperature gradient of $Ra_T = 161\,560$, the experimental value. Since the overall stable density gradient is reduced by heating, it is anticipated that the instability island will be reduced in area.

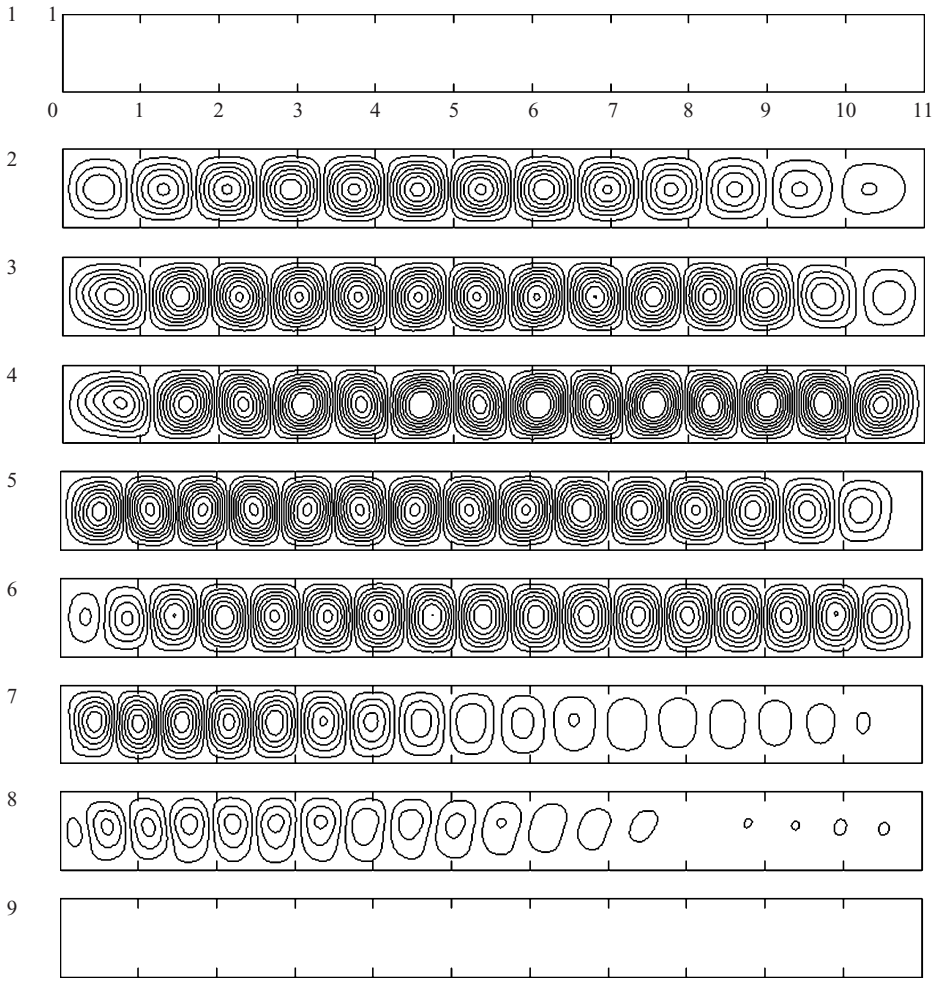

FIGURE 22. Sequence of streamline patterns within the instability island shown in figure 21(*b*) at $\omega_m = 240.1$. 1, $t = 1.0$, $\Delta\psi = \pm 0.0125$; 2, $t = 2.0$, $\Delta\psi = \pm 0.0313$; 3, $t = 3.0$, $\Delta\psi = \pm 1.125$; 4, $t = 4.0$, $\Delta\psi = \pm 1.125$; 5, $t = 6.0$, $\Delta\psi = \pm 1.125$; 6, $t = 8.0$, $\Delta\psi = \pm 0.50$; 7, $t = 9.0$, $\Delta\psi = \pm 0.25$; 8, $t = 10.0$, $\Delta\psi = \pm 0.025$; 9, $t = 11.0$, $\Delta\psi = \pm 0.0125$.

As shown in figure 21(*b*), the critical frequency range is reduced approximately by half to $180 \leqslant \omega_m \leqslant 300$, and the unstable time interval only extends to $t = 30$. Beyond the critical time period, the fluid layer reverts back to the stable state. It remains stable until the solute gradient becomes too low to resist the adverse effects of the thermal gradient and causes the onset of double-diffusive instability at $t \approx 60$. In the figure, this stability boundary is marked by open circles. In the range of modulation frequency $180 \leqslant \omega_m \leqslant 300$, owing to the additional reduction of the stable solutal gradient by the internal wave mode of instability, the onset of double-diffusive instability occurs slightly earlier than it would otherwise. The onset motion still consists of two rows of vortices similar to those shown in figure 16.

The fluid motion within the internal wave instability region is illustrated by a sequence of streamline contours at $\omega_m = 240.1$ and $1 \leqslant t \leqslant 11$ in figure 22. It shows that the instability motion consists of a single row of oscillating vortices whose strength

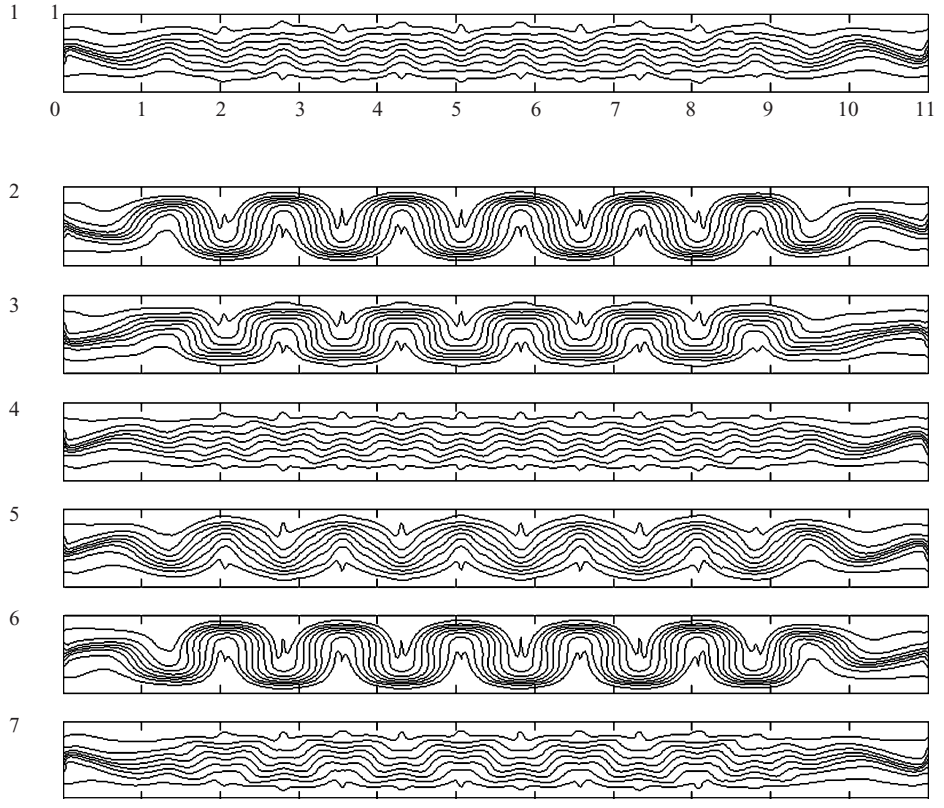

FIGURE 23. Displacement of concentration contours by the cyclic internal wave motions of the instability in the example shown in figure 22. 1, $t = 3.075$, 2, $t = 3.085$, 3, $t = 3.095$, 4, $t = 3.100$, 5, $t = 3.105$, 6, $t = 3.115$, 7, $t = 3.125$.

first increases then decreases with time as the solute gradient becomes weaker and eventually returns to the quiescent state. The internal wave nature of this unstable motion can be illustrated clearly by setting a horizontal dyeline in the experimental tank, or by the lines of constant solute concentration from the simulation results over a cycle of oscillation. A sequence of seven plots of such concentration contours over a cycle, $3.075 \leqslant t \leqslant 3.125$, is presented in figure 23. The cyclic wave motion is clearly exhibited. These waves will persist, but with diminishing amplitude as t approaches 11 and then vanish completely for $t > 11$ as the fluid layer becomes stable. In the subsequent double-diffusive instability, wave motion will first appear immediately after onset, but these waves will break when the solute gradient is destroyed by the mixing process.

Figure 21(b) shows that there is another larger reduction in the time of onset of the double-diffusive instability at low modulation frequencies, $\omega_m \leqslant 120$. This is a manifestation of the resonant instability effect of a double-diffusive layer under gravity modulation shown by Saunders *et al.* (1992). They showed that the resonant bands centre at modulation frequencies $\omega_m \approx 2\sigma_i/m$, where m is an integer and σ_i is the critical onset frequency at steady gravity. The fundamental resonant band, $m = 1$, is in the subharmonic mode and effects the most destabilization. According to linear stability analysis for a sinusoidal solute distribution (see figure 13), the oscillation frequency at the critical state is $\sigma_i = 27.1$. Figure 21(b) shows that the destabilized

region as indicated by the reduction in the time of instability onset centres at $\omega_m \approx 2\sigma_i$. When the modulation amplitude is increased to $g_1 = 1.0$, the internal wave mode of instability is enlarged to such an extent that the stability boundaries of the two modes intersect.

8. Conclusions

We have successfully devised an experimental method to study the instability onset process in a horizontal stratified fluid layer enclosed in a rigid tank being heated from below both under steady gravity and gravity modulation. We formulated a two-dimensional numerical method to simulate the behaviour of the fluid layer under the experimental test conditions. A linear stability analysis was also applied to the same problem with a nonlinear solute distribution. From the results of these studies, the following conclusions can be drawn.

1. Under steady gravity, the predictions of the critical conditions at instability onset based on the linear stability theory and the two-dimensional simulations agree very well with the experimental results, with relative errors of less than 3 %. The earlier experimental results of Shirtcliff (1967, 1969) and Wright & Loehrke (1976) also show good agreement with linear stability theory. The nonlinear evolution of the fluid motion from the instability onset to the final thermal convection state as predicted by nonlinear simulations is very similar to that observed in the experiments.

2. For ideal sinusoidal variations of the gravity at 1 Hz with amplitude of $0.41g$, both linear theory and two-dimensional simulations predict no change in the critical conditions for instability onset. The nonlinear evolution of the instability motion as predicted by two-dimensional simulations is similar to that under steady gravity.

3. Under the actual gravity modulation as generated by the oscillating platform, both the experiments and the two-dimensional simulations show that the fluid layer becomes less stable with increases in the critical solute Rayleigh number, Ra_S, and the oscillation frequency at onset, f_{onset}, from their respective values at steady gravity. However, the increases in the simulation values are modest as compared to the increases obtained in the experiments. Simulation results show an increase of 1.4 % in Ra_S and 8.9 % in f_{onset}. In the experiments, the corresponding values are 8.4 % and 32.6 %.

4. Analysis of the work components contributing to the time rate of change of the kinetic energy shows that during the onset process, all terms exhibit growing oscillations at twice the onset frequency. Under steady gravity, the changes in the kinetic energy are mainly due to the difference between the net buoyancy work and the dissipation resulting from the shear work. The contribution of the pressure work is negligible. Under ideal gravity modulation, an oscillation of small amplitude at the modulation frequency is superposed on the growth curves. In this case, the changes in the kinetic energy are mainly due to the work of the unsteady pressure.

5. The possibility of encountering an internal wave mode of instability in an experimental set-up such as ours has been demonstrated with our two-dimensional simulation code. For the experimental solute-stratified fluid layer without heating, such instability can be excited at a lower modulation frequency (0.35–0.68 Hz) and higher amplitude ($0.75g$) than those in the experiment. After onset, the instability motion first grows in strength and then slowly decays as the background solute gradient is diminishing. The wave nature of the instability is illustrated by the motion of the constant solute contours over a cycle of oscillation. Eventually, the wave subsides and the layer returns to the stable state. The instability is confined within a closed region

in the time-frequency domain. When a destabilizing temperature gradient is imposed on the layer, the occurrence of internal waves destabilizes the fluid layer with respect to the double-diffusive instabilities.

The financial support provided by NASA Grant NAG3-2354 for this research is gratefully acknowledged. We thank Dr Stuart Dalziel for alerting us to the possibility of internal wave instability in our experiment.

REFERENCES

Arakawa, A. 1966 Computational design for long-term numerical integration of the equations of fluid motion: two-dimensional incompressible flow. Part 1. *J. Comput. Phys.* **1**, 119–143.

Benielli, D. & S ommeria, J. 1998 Excitation and breaking of internal gravity waves by parametric instability. *J. Fluid Mech.* **374**, 117–144.

Chan, C. L., Yu, Y. & Chen, C. F. 2004 Instability of convection of an ethanol–water solution in a vertical tank. *J. Fluid Mech.* **510**, 243–265.

Chen, W.-Y. & Chen, C. F. 1999 Effect of gravity modulation on the stability of convection in a vertical slot. *J. Fluid Mech.* **395**, 327–344.

DuFort, E. C. & Frankel, S. P. 1953 Stability conditions in the numerical treatment of parabolic differential equations. *Math. Tables Other Aids Comput.* **7**, 135–152.

Gershuni, G. Z., Zhukhovitskii, E. M. & Iurkov, I. S. 1970 On the convective stability in the presence of periodically varying parameter. *Z. Angew. Math. Mech.* **34**, 442–452.

Ghorayeb, K. & Mojatabi, A. 1997 Double diffusive convection in a vertical rectangular cavity. *Phys. Fluids* **9**, 2339–2348.

Gresho, P. M. & Sani, R. L. 1970 The effects of gravity modulation on the stability of a heated fluid layer. *J. Fluid Mech.* **40**, 783–806.

Hayes, M. H. 1996 *Statistical Digital Signal Processing and Modeling*. Wiley.

Houstis, E. N. & Papatheodorou, T. S. 1979 High-order fast elliptic equation solvers. *ACM Trans. Math. Software* **5**, 431–441.

Huang, H. & Wetton, B. R. 1996 Discrete compatibility in finite difference methods for viscous incompressible fluid flow. *J. Comput. Phys.* **126**, 468–478.

Huppert, H. E. & Moore, D. R. 1976 Nonlinear double-diffusive convection. *J. Fluid Mech.* **78**, 821–854.

Landolt, H. & Bornstein, R. 1989 *Eigenschaften der Materie in ihren aggregatzustaden*, part 5, p. 640. Springer.

Napolitano, M., Pascazio, G. & Quartapelle, L. 1999 A review of vorticity conditions in the numerical solution of the ζ–ψ equations. *Computers Fluids* **28**, 139–185.

Nield, D. A. 1967 The thermohaline Rayleigh–Jeffreys problem. *J. Fluid Mech.* **29**, 545–558.

Proakis, J. G. & Manolakis, D. G. 1996 *Digital Signal Processing: Principles, Algorithms, and Applications*. Prentice–Hall.

Roache, P. J. 1982 *Computational Fluid Dynamics*. Hermosa, Albuquerque, NM.

Rogers, J. R., Pesch, W., Brausch, O. & Schatz, M. F. 2005 Complex-ordered patterns in shaken convection. *Phys. Rev.* E **71**, 066214-1-18.

Saunders, B. V., Murray, B. T., McFadden, G. B., Coriell, S. R. & Wheeler, A. A. 1992 The effect of gravity modulation on thermosolutal convection in an infinite layer of fluid. *Phys. Fluids* A **4**, 1176–1189.

Sekerzh-Zen'kovich, S. Ya. 1983 Parametric resonance in a stratified liquid in a container undergoing vertical vibration. *Sov. Phys. Dokl.* **28**(6), 445–446.

Shirtcliffe, T. G. L. 1967 Thermosolutal convection: observation of an overstable mode. *Nature* **213**, 489–490.

Shirtcliffe, T. G. L. 1969 An experimental investigation of thermosolutal convection at marginal stability. *J. Fluid Mech.* **35**, 677–688.

Sinha, S. C. & Wu, D.-H. 1991 An efficient computational scheme for the analysis of periodic systems. *J. Sound Vib.* **151**, 91–117.

Tanny, J., Chen, C. C. & Chen, C. F. 1995 Effects of interaction between Marangoni and double-diffusive instabilities. *J. Fluid Mech.* **303**, 1–21.

Turner, J. S. 1973 *Buoyancy Effects in Fluids*. Cambridge University Press.

Wright, J. H. & Loehrke, R. I. 1976 The onset of thermohaline convection in a linearly-stratified horizontal layer. *Trans. ASME* C: J. Heat Transfer **98**, 558–563.